Short-range and long-range order of phyllomanganate nanoparticles determined using high-energy X-ray scattering
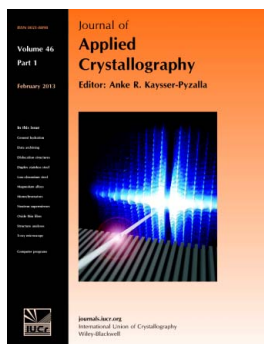
Alain Manceau, Matthew A. Marcus, S. Grangeon, M. Lanson, B. Lanson, A.-C. Gaillot, S. Skanthakumar and L. Soderholm

Journal of Applied Crystallography covers a wide range of crystallographic topics from the viewpoints of both techniques and theory. The journal presents papers on the application of crystallographic techniques and on the related apparatus and computer software. For many years, the *Journal of Applied Crystallography* has been the main vehicle for the publication of small-angle scattering papers and powder diffraction techniques. The journal is the primary place where crystallographic computer program information is published.

Crystallography Journals Online is available from **journals.iucr.org**

Short-range and long-range order of phyllomanganate nanoparticles determined using high-energy X-ray scattering

Alain Manceau,[a]* Matthew A. Marcus,[b] S. Grangeon,[a]‡ M. Lanson,[a] B. Lanson,[a] A.-C. Gaillot,[c] S. Skanthakumar[d] and L. Soderholm[d]

[a]ISTerre, CNRS and Université de Grenoble 1, 38041 Grenoble Cedex 9, France, [b]Advanced Light Source, Lawrence Berkeley National Laboratory, One Cyclotron Road, Berkeley, CA 94720, USA, [c]Institut des Matériaux Jean Rouxel (IMN), Université de Nantes, CNRS, 2 Rue de la Houssinière, BP 32229, 44322 Nantes Cedex 3, France, and [d]Chemical Sciences and Engineering Division, Argonne National Laboratory, CHM/200, 9700 South Cass Avenue, Argonne, IL 60439, USA. Correspondence e-mail: manceau@ujf-grenoble.fr

High-energy X-ray scattering (HEXS) is used to explore the pH-dependent structure of randomly stacked manganese oxide nanosheets of nominal formula δ-MnO$_2$. Data are simulated in real space by pair distribution function (PDF) analysis and in reciprocal space by both the Bragg-rod method and the Debye equation in order to maximize the information gained from the total scattering measurements. The essential new features of this triple-analysis approach are (1) the use of a two-dimensional supercell in PDF modeling to describe local distortions around Mn layer vacancies, (2) the implementation in Bragg-rod calculations of a lognormal crystal size distribution in the layer plane and an empirical function for the effect of strain, and (3) the incorporation into the model used with the Debye equation of an explicit elastic deformation of the two-dimensional nanocrystals. The PDF analysis reveals steady migration at acidic pH of the Mn atoms from layer to interlayer sites, either above or below the Mn layer vacancies, and important displacement of the remaining in-layer Mn atoms toward vacancies. The increased density of the vacancy–interlayer Mn pairs at low pH causes their mutual repulsion and results in short-range ordering. The layer microstructure, responsible for the long-range lateral disorder, is modeled with spherically and cylindrically bent crystallites having volume-averaged radii of 20–40 Å. The b unit-cell parameter from the hexagonal layer has different values in PDF, Bragg-rod and Debye equation modeling, because of the use of different weighting contributions from long-range and short-range distances in each method. The PDF b parameter is in effect a measure of the average inlayer Mn$\cdots$Mn distance and consistently deviates from the average structure value determined by the Bragg-rod method by 0.02 Å at low pH, as a result of the local relaxation induced by vacancies. The layer curvature increases the Bragg-rod value by 0.01–0.02 Å with the cylindrical model and as much as 0.04–0.05 Å with the spherical model. Therefore, in principle, the diffraction alone can unambiguously determine with good accuracy only a volume-averaged apparent layer dimension of the manganese oxide nanosheets. The b parameter is model dependent and has no single straightforward interpretation, so comparison of b between different samples only makes sense if done in the context of a single specified model.

1. Introduction

Manganese oxide nanosheets, of nominal formula δ-MnO$_2$, are the most common natural form of manganese and have emerged as interesting new materials for energy storage (Li/

MnO$_2$ batteries), photoelectric conversion, chemical separation (ion and molecular sieves), heterogeneous catalysis and hazardous waste remediation (Thackeray, 1997; Brock et al., 1998; Feng et al., 1999; Toupin et al., 2004; Wang et al., 2004, 2005; Sakai et al., 2005; Laatikainen et al., 2010; Lafferty et al., 2010; Nakayama et al., 2010; Tang et al., 2010; Cormie et al., 2010; Yan et al., 2010; Simonin et al., 2012; Yu et al., 2012).

‡ Present address: BRGM, 2 Avenue Claude Guillemin, 45060 Orléans Cedex 2, France.

193

Recently, a layered $Mn^{III/IV}$ nanomanganate similar to that made by Mn-oxidizing bacteria has been shown to be an effective photocatalyst for water splitting (Hocking *et al.*, 2011; Weichen *et al.*, 2012; Zaharieva *et al.*, 2012). Despite the importance of biogenic and chemical MnO_2 nanosheets, their structure has been described thus far only in terms of a 'periodic' arrangement of lattice planes using space-group symmetries (Jürgensen *et al.*, 2004; Villalobos *et al.*, 2006; Lanson *et al.*, 2008; Grangeon *et al.*, 2008, 2010, 2012). Many details of their defect structure, which defines their reactivity and stability to a large extent, are unknown.

Three main known characteristics of MnO_2 nanosheets are the presence of manganese vacancies, substitutions of Mn^{3+} for Mn^{4+} and the curling of layers as a result of weakened interlayer interactions caused essentially by the high concentration of defects (Fig. 1). Theoretically, high-energy X-ray scattering (HEXS) permits short-range and long-range order determination with improved structural resolution. However, full-profile HEXS analysis of two-dimensional crystals is difficult for several reasons. The diffraction pattern exhibits only broadened $hk0$, 001 and 002 peaks, and no hkl with $|hk| \neq 00$, $l \neq 0$, because stacked layers are uncorrelated in position and orientation (Drits *et al.*, 1984; Drits, Silvester *et al.*, 1997). Turbostratic disorder in the **c** direction, added to finite domain size, strain and point defects within the crystal *ab* plane, strongly modifies diffraction line profiles and leads to asymmetrical broadening and peak shifting (Drits & Tchoubar, 1990; Lanson *et al.*, 2000; Lanson, Drits, Gaillot *et al.*, 2002; Casas-Cabanas *et al.*, 2007). The complex diffraction pattern cannot be modeled as simple overlap of size-broadened 'Bragg' reflections using standard Rietveld-like methods (Rietveld, 1969; Cheary & Coelho, 1992). These difficulties directly lead to questions of the best way to analyze HEXS data for this type of material, and specifically, whether computer simulations should be compared with data in real or reciprocal space (Egami & Billinge, 2003; Beyerlein *et al.*, 2009). There are advantages and disadvantages to each approach.

Fourier transformation of the total scattering pattern provides direct visualization of the radial distribution of the atomic pair density over several tens of ångströms, and often allows intuitive interpretations from complementary information (obtained by EXAFS spectroscopy, for instance) (Billinge & Kanatzidis, 2004; Neder & Korsunskiy, 2005; Skanthakumar *et al.*, 2007; Soderholm *et al.*, 2008; Krayzman *et al.*, 2008; Proffen & Kim, 2009). Local atomic arrangements on the nanometre length scale, and in favorable cases intermediate to long-range order, can be obtained by fitting of the pair distribution function (PDF), whereas refinements in reciprocal space yield only the long-range average structure. The finite size of nanocrystals does not broaden features in real space but instead causes progressive vanishing of the pair maxima with increasing radial distance. For δ-MnO_2, this effect is observed at $r \geq \sim 7.2$ Å, which is the layer-to-layer separation. Modeling of the PDF at a higher radial distance is complex for the two main reasons described below.

First, the PDF is fitted to a bulk model periodic in three dimensions, whereas layered nanomaterials are strictly periodic in only two dimensions. When the proportion of stacking faults is less than approximately 50%, a good pattern fit can still be obtained by introducing anisotropic displacement parameters (ADPs), in which values related to the out-of-plane **c** direction (U_{33}) are increased to reduce layer–layer correlations (Petkov *et al.*, 2002; Masadeh *et al.*, 2007). Completely random stacking was simulated for pyrolytic graphite by enlarging the ADPs in the **c** direction and artificially multiplying the model PDF with a broad Gaussian function to reproduce the persistent loss of structural coherence occurring at distances greater than the interslab separation (Petkov *et al.*, 1999). Similarly, the use of a modified error function (integrated Gaussian) has been used for quantitative treatment of coordination-environment disordering about a metal ion in an aqueous solution (Soderholm *et al.*, 2009).

Second, analytical expressions of the form factor used to describe the shape and size of the crystallites are available for some simple geometrical forms (*e.g.* spherical, spheroidal, cyclindrical) but not for two-dimensional nanoparticles (Gilbert, 2008; Lei *et al.*, 2009). Further complications are that diffracting domains do not necessarily have well defined
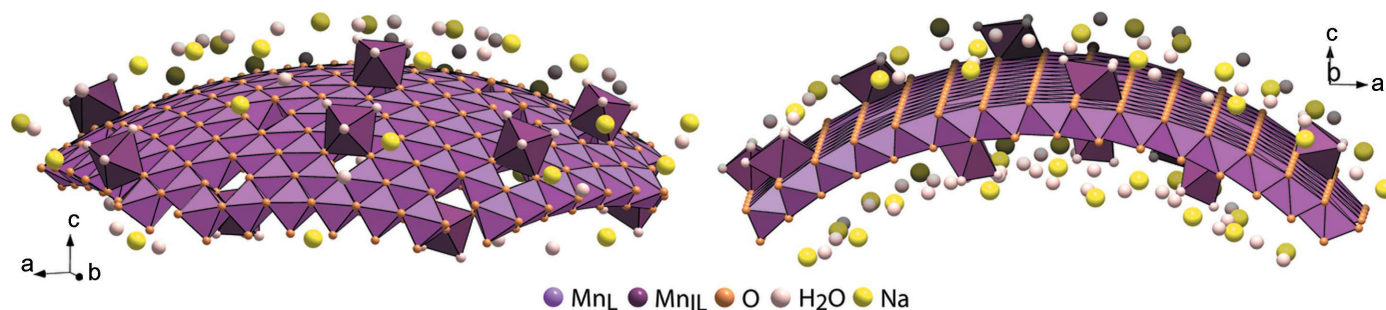

Mn$_L$ Mn$_{IL}$ O   H$_2$O   Na

Figure 1
Short-range and long-range order structure of a δ-MnO_2 monolayer at pH 10 (dBi10) as derived from PDF, Bragg-rod and Debye equation modeling of HEXS data. The octahedral layer contains 79 at.% Mn^{4+} and 11 at.% Mn^{3+} (Mn_L), and 10% vacancies which for the most part (8%) are capped by an interlayer Mn^{3+} octahedron (Mn_{IL}). The Mn_{IL} octahedra share three corners (TCS bonding) with the three surface O atoms surrounding a vacancy, and complete their coordination with three interlayer water molecules. The layer charge deficit created by Mn^{4+} vacancies and Mn_{IL}^{3+} for Mn_L^{4+} substitutions is compensated by 8 at.% Mn_{IL}^{3+}, 27 at.% Na^+ and H^+ (not represented). The interlayer also contains water molecules weakly bonded to Na. The microstructure of the nanosheet can be described equally well with a spherical (left) or cylindrical (right) bend.

shapes or similar sizes, probably have irregular edges, and certainly have non-uniform strain. Representing a nanofilm with a three-dimensional shape function modifies the relative intensities of atomic pairs and introduces strong correlations between disorder and crystallographic parameters, especially at intermediate to long distances where diffuse scattering from nanosized grains provides a large contribution to the PDF (Gilbert, 2008; Lei et al., 2009; Petkov, Cozzoli et al., 2009). Therefore, the presumption of a unit cell repeated in three-dimensional space, which is the basis of full-pattern fitting of PDFs, a sort of 'real-space Rietveld' method, breaks down for the structural analysis of layered nanoparticles.

As an alternative to the PDF, HEXS data of two-dimensional crystals can be described in terms of the scattering from individual layers using the Bragg-rod formalism (Plançon, 1981; Drits & Tchoubar, 1990; Shi et al., 1993; Yang & Frindt, 1996a; Leoni, 2008) or by atom pairs using the Debye equation (Debye, 1915; Yang & Frindt, 1996b). In the first approach, layers are considered to be finite-size pieces of periodic two-dimensional crystals. As a result of their two-dimensional nature, they produce rods of intensity in q space [the magnitude of the scattering vector $q = (4\pi/\lambda)\sin\theta$, where θ is half the scattering angle and λ is the wavelength of the incident radiation]. These rods are broadened by the finite size of the layers and modulated in the $\mathbf{c}^*$ direction by any correlation between layers. If these rods are narrow enough in the in-plane direction to be non-overlapping, then the Bragg-rod formalism may be used. Analytical expressions of the shape function are known for various geometries of the two-dimensional domains (circle and polygons), and size distributions (generally lognormal; Drits, Srodon & Eberl, 1997; Langford et al., 2000) can be computed by varying the domain size iteratively. However, when Bragg-rod calculations are carried out, it often appears necessary to assume coherent scattering domains (CSDs), which become smaller for higher-order reflections. This effect was explained by Drits & Tchoubar (1990) as being caused by non-uniform strain but was never modeled specifically because the q range accessible by conventional powder diffraction is too short ($q_{max} < \sim5$ Å^{-1}) to characterize all structural imperfections. Although HEXS does not have this experimental limitation and may support more complex Bragg-rod models, anisotropic elasticity in two-dimensional crystals is much easier to describe in the Debye formalism.

The Debye equation (Debye, 1915; Yang & Frindt, 1996b) expresses the diffracted intensity as a sum over contributions from all atomic pairs in the solid without any assumptions regarding the periodic nature of the scattering object and therefore is a more direct way of calculating the powder pattern of finite structures. All that is needed is an explicit list of all interatomic distances r_{ij} contained in the model. From a crystallographic standpoint, it is a superior method for the analysis of nanoparticles, because all structural parameters, such as atomic arrangement, relaxation effects, stacking faults, size, shape, anisotropic strain and other inhomogeneities, are intrinsic parameters of the particle's input atomic structure and hence are directly accessible to modeling. The modeled

structural defects are physically present in the structure (Oddershede et al., 2008) and not introduced in an approximate or artificial way. With respect to site occupancies, it is possible to build models in such a way that for a given atom there is a distance-dependent probability of another atom of the same type being located a given number of sites away. The atom may or may not be present, but may not be described as being 'half there', as a fractional occupancy in the PDF and Bragg-rod approaches might seem to suggest. In addition, site occupancies are correlated in that, if one atom is present, other atoms must be either present or absent. For instance, if an interlayer Mn atom (Mn_{IL}) is present above a layer vacancy, then so too must its coordinating oxygen atoms from the layer and water molecules that extend out into the interlayer (Fig. 1). In addition, no two vacancies can be neighbors, and the layer site (Mn_L) below Mn_{IL} should be unoccupied. Similarly, there can be steric conflicts in the interlayer, so that some sets of atoms cannot be present at the same time. All these constraints can be controlled with a suitable algorithm for distance sampling, with the caveat that the approach is deterministic and hence requires many configurations of the same atomic model to be generated to smooth out statistical fluctuations. Also, each iteration aimed at optimizing the model structure is computationally costly because the diffracted intensity is calculated numerically for all atomic pairs at every q value (Oddershede et al., 2008). The computation time is quadratic in the number of atoms (Gelisio et al., 2010). For these reasons, the Debye equation (DE) method has been applied only once to HEXS data, for the analysis of the size distribution and anisotropic shape of TiO_2 nanocrystals (Cernuto et al., 2011). Strain analysis was not attempted in this previous study, and no anisotropic strain model has yet been added to the Debye equation.

On the basis of these considerations, there is no single appropriate method for modeling highly disordered two-dimensional nanocrystals, partly for theoretical reasons (some structural features have no simple analytical description) and partly for data analysis reasons. Therefore, the total scattering of δ-MnO_2 is modeled for the first time using a triple-analysis approach. The relaxation of layer Mn sites, induced by vacancies, and the site occupation, occupancy and short-range ordering of interlayer Mn, are described first from the simulation of the PDF over a range of 7.0–7.2 Å using a two-dimensional supercell. The Bragg-rod approach is used next to determine average lattice parameters, calculate the lognormal distribution of particle sizes and evaluate empirically the importance of anisotropic strain using a phenomenological q-dependent broadening function. The elasticity of the nanocrystals is described more accurately in the third phase of the analysis with spherical and cylindrical 'mandrel' models implemented in the Debye equation.

2. Experimental

2.1. Samples

A suspension of Na-saturated δ-MnO_2 was prepared in 2006 in alkaline medium (pH $\simeq$ 8) following the 'redox' method

Table 1
Chemical and structural formulae of the δ-MnO$_2$ samples.

Na was measured by ICP–AES analysis, the Mn^{3+}/Mn^{4+} ratio by potentiometric titration, and strongly sorbed water by TGA. Analyses were performed one month after synthesis.

pH 10 – dBi10	
Chemical	$Na_{0.27}Mn^{3+}_{0.19}Mn^{4+}_{0.81}O_2 \cdot 0.3H_2O$
Structural	$[Na^+_{0.27}(H_2O)_{0.30}Mn^{3+}_{0.08}(H_2O)_{0.24}]_{IL}(Mn^{4+}_{0.79}Mn^{3+}_{0.11}\square_{0.10})_LO_2$
pH 6 – dBi6	
Chemical	$Na_{0.18}Mn^{3+}_{0.27}Mn^{4+}_{0.73}O_2 \cdot 0.3H_2O$
Structural	$[H^+_{0.16}Na^+_{0.18}(H_2O)_{0.30}Mn^{3+}_{0.15}(H_2O)_{0.45}]_{IL}(Mn^{4+}_{0.72}Mn^{3+}_{0.11}\square_{0.17})_LO_2$
Structural†	$[H^+_{0.10}Na^+_{0.18}(H_2O)_{0.30}Mn^{3+}_{0.13}(H_2O)_{0.39}]_{IL}(Mn^{4+}_{0.75}Mn^{3+}_{0.11}\square_{0.14})_LO_2$
pH 3 – dBi3	
Chemical	$Na_{0.06}Mn^{3+}_{0.31}Mn^{4+}_{0.69}O_2 \cdot 0.3H_2O$
Structural	$[H^+_{0.18}Na^+_{0.06}(H_2O)_{0.30}Mn^{3+}_{0.21}(H_2O)_{0.63}]_{IL}(Mn^{4+}_{0.70}Mn^{3+}_{0.11}\square_{0.19})_LO_2$

† Interpolated from pH 3 and 10.

(Villalobos *et al.*, 2003) adjusted to a molar ratio of KMnO$_4$ to MnCl$_2$ of 0.67. The suspension was split into three batches, equilibrated at pH 10 (dBi10), 6 (dBi6) and 3 (dBi3). These samples were filtered and rinsed with deionized water, and the powder freeze dried and stored under ambient conditions for further analysis. It took two hours to equilibrate the suspension at pH 6 and five hours at pH 3. Drops of highly diluted suspensions were deposited on holey carbon-coated Cu grids for transmission electron microscopy (TEM) imaging. Observations were performed on a Hitachi H9000NAR transmission electron microscope equipped with an LaB$_6$ electron source operated at 300 kV. At low and intermediate magnification, the crystals appear like crumpled sheets of newspaper (Fig. 2a). Aggregates of euhedral hexagons of 5–30 nm in transverse dimension are observed at high magnification, occasionally with folded borders (Figs. 2b and 2c). Observed perpendicularly to the layer plane, the crystals appear to be composed of about two–five nanosheets with a layer-to-layer distance of ∼7 Å. They are systematically curved and occasionally knee-bent (arrows in Fig. 2c). The long branch of the Y-shaped nanocrystal shown in Fig. 2(c) has a radius of curvature of 70 Å and the acute angle an approximate radius

of 10 Å. Its nanosheets appear corrugated, similarly to those from the folded border of the euhedral crystal in Fig. 2(b).

Omitting protonated surface sites at crystal edges, the generic formula of the Mn oxide nanosheets is $[H^+_nNa^+_v(H_2O)_wMn^{3+}_x(H_2O)_{3x}]_{IL}(Mn^{4+}_{1-y-z}Mn^{3+}_y\square_z)_LO_2$, where the negative charge of the layer (L) resulting from Mn^{3+} for Mn^{4+} substitutions and octahedral vacancies ($\square$) is compensated for by interlayer (IL) cations (Table 1). The Na content was obtained by wet chemical analysis (inductively coupled plasma atomic emission spectroscopy, ICP–AES), the amount of strongly sorbed water (w) from the weight loss between 373 and 513 K as measured by thermogravimetric analysis (TGA) (Feng *et al.*, 1998; Gaillot *et al.*, 2003; Villalobos *et al.*, 2006), the Mn$^{3+}_L$ content (y) from x, z, and the Mn^{3+}/Mn^{4+} ratio by potentiometric titration (Grangeon *et al.*, 2012). One of the objectives of this study is to determine the fractional amounts of Mn$_{IL}$ (x) and layer vacancies (z).

In addition to the three δ-MnO$_2$ samples, two birnessites (well crystallized phyllomanganates), whose crystal structure has been solved by X-ray diffraction to the requisite level of detail, are analyzed by the PDF method, first to evaluate the sensitivity of this technique to the layer and interlayer structure of phyllomanganates, and second to devise from this result an optimal fitting strategy for the analysis of the δ-MnO$_2$ nanocrystals. The first reference (KBi8) is a K-rich birnessite synthesized at 1073 K of formula $[K^+_{0.231}(H_2O)_{0.36}Mn^{3+}_{0.077}(H_2O)_{0.24}]_{IL}(Mn^{4+}_{0.885}\square_{0.115})_LO_2$. Its periodic structure has been refined from single-crystal X-ray diffraction (XRD) data and its defect structure by the analysis of powder data (Gaillot *et al.*, 2003). The layer contains only Mn^{4+} cations and therefore has hexagonal symmetry (space group $P6_3/mmc$ with $a = b = 2.845$ Å). The few Mn^{3+} cations are positioned in the interlayer above or below Mn^{4+} layer vacancies. Interlayer K$^+$ cations and H$_2$O molecules occupy three symmetry-equivalent sites, located above the tridentate layer cavities for K and above the octahedral faces for H$_2$O (Fig. 3). Layers are stacked regularly with a 2H periodicity in defect-free crystals and with a 2H and 3R sequence in defective crystals. The 2H and 3R fragments are randomly interstratified with a mean
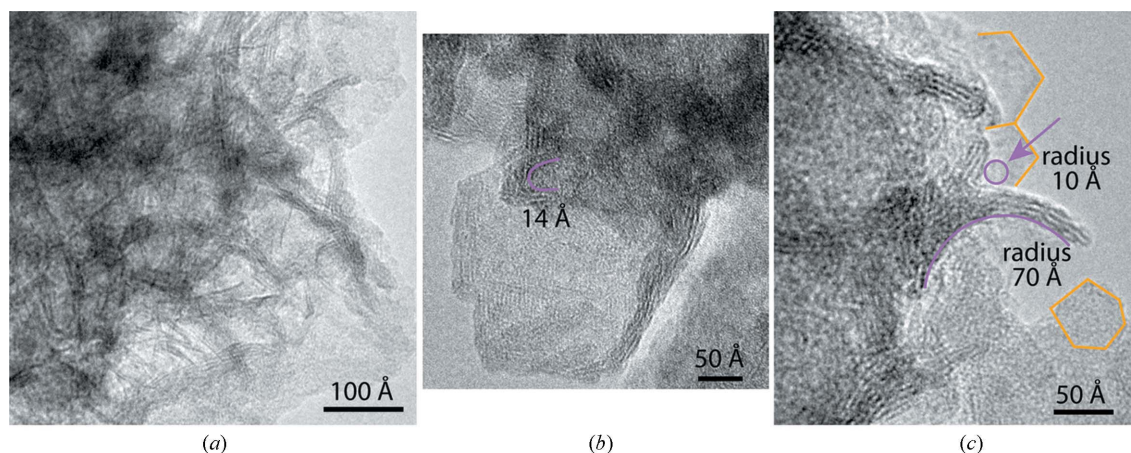

Figure 2
Electron micrographs of δ-MnO$_2$ nanoparticles. (a) Intermediate-magnification image of curled particles viewed edge on. The particles contain two–five layers. (b) High-magnification view of a hexagonal crystal folded on one edge and revealing the type of lattice fringes shown in (a). The U-shaped crystallite has a radius of curvature of 14 Å. (c) High-magnification image of hexagonal crystals viewed parallel and perpendicular to the layer plane.

occurrence probability of 60:40% and an average CSD dimension along the **c** direction of ten layers.

The second reference is an Na-rich birnessite (NaBi) synthesized at room temperature in alkaline medium, then aged hydrothermally at 423 K (Drits, Silvester *et al.*, 1997; Silvester *et al.*, 1997; Lanson, Drits, Feng & Manceau, 2002). Its average formula is $[(Na^+_{0.31}(H_2O)_{0.4})_{IL}(Mn^{4+}_{0.69}Mn^{3+}_{0.31})_L]O_2$. The layer Mn^{3+} octahedra all have the same azimuthal elongation and are ordered into stripes along the **b** direction separated by two Mn^{4+} rows in the perpendicular direction (Fig. 3). The ordering of the Mn^{3+} cations lowers the layer symmetry from hexagonal to orthogonal (space group $P\bar{1}$ with $a = 5.174$, $b = 2.848$ Å, $a/b = 1.817$), and splits the $Mn\cdots Mn$ distances across octahedral edges. The $Mn\cdots Mn$ separation increases radially with distance from 2.85–2.95 Å for the Mn1 shell, to 7.57–7.89 Å for the Mn4 shell, and to 9.98–10.74 Å for the overlapping Mn6 and Mn7 shells. For comparison, the Mn atoms are all at 7.51, 9.84 and 10.24 Å in the Mn4, Mn6 and Mn7 shells of KBi8. The NaBi sample contains two types of crystals, which differ in the amount and distribution of heterovalent Mn in the Mn^{3+}-rich rows, with effects on the periodicity of interlayer Na and H_2O generating modulated structures.

2.2. High-energy X-ray diffraction measurement and data reduction

Data were collected 24 months after synthesis at the Advanced Photon Source (APS) on beamline 11-ID-B with an X-ray energy of 90.480 keV (λ = 0.13702 Å). The aged samples were enclosed in Kapton capillaries with epoxy plugs, and the diffracted intensities were measured in transmission from q = 0.2 to 32 Å^{-1} with an image plate and corrected for incomplete absorption in the phosphor (Zaleski *et al.*, 1998). Geometric corrections were made with *Fit2D* (Hammersley *et al.*, 1996) using CeO_2 as standard, and the background contribution was calculated from data collected on empty tubing. The total scattering structure function, $S(q)$, was obtained as described previously (Skanthakumar & Soderholm, 2006), and the PDF was calculated by integration of the reduced structure function $F(q)$ (Egami & Billinge, 2003; Billinge & Kanatzidis, 2004) over the $0.2 \leq q \leq 24$ Å^{-1} (KBi8 and NaBi) and $0.2 \leq q \leq 29$ Å^{-1} (dBi) intervals.

2.3. PDF analysis

The PDFs were fitted with *PDFgui* (Farrow *et al.*, 2007) to

$r_{max} = 40$ Å for the two crystalline references and to 7.0–7.2 Å for δ-MnO_2, because this program does not deal with disc- or lath-like CSDs or anisotropic strain effects. Several model fits were attempted to determine a minimal set of constraints and evaluate the fitting precision on structural parameters. A fit was considered reliable when all parameters were physically and structurally meaningful and correlations between parameters were lower than 0.8. Although somewhat arbitrary, this value corresponds to the hard-coded *PDFgui* threshold below which the refinement parameters are considered independent. To satisfy these requirements, the ADPs of all interlayer species had to be modeled isotropically (U_{iso}). Allowing O_L and Mn_L to move anisotropically along the **c** direction (U_{33}) and isotropically in the layer plane ($U_{11} = U_{22}$) much improved the fits without introducing parameter correlations. The soundness of this approach for the simulation of c-disordered layered Mn oxides has already been demonstrated (Gateshki *et al.*, 2004). The occupancies of Na/K and water molecules were fixed to their stoichiometric values, and the Mn_L and Mn_{IL} cation occupancies were linked according to layer–interlayer charge balance, omitting protons and considering that all Mn_{IL} were trivalent and Mn_L tetravalent (Villalobos *et al.*, 2006; Zhu *et al.*, 2012).

2.4. Bragg-rod analysis

The HEXS patterns were modeled with *CALCIPOW* (Plançon, 2002), using atomic form factors for neutral atoms
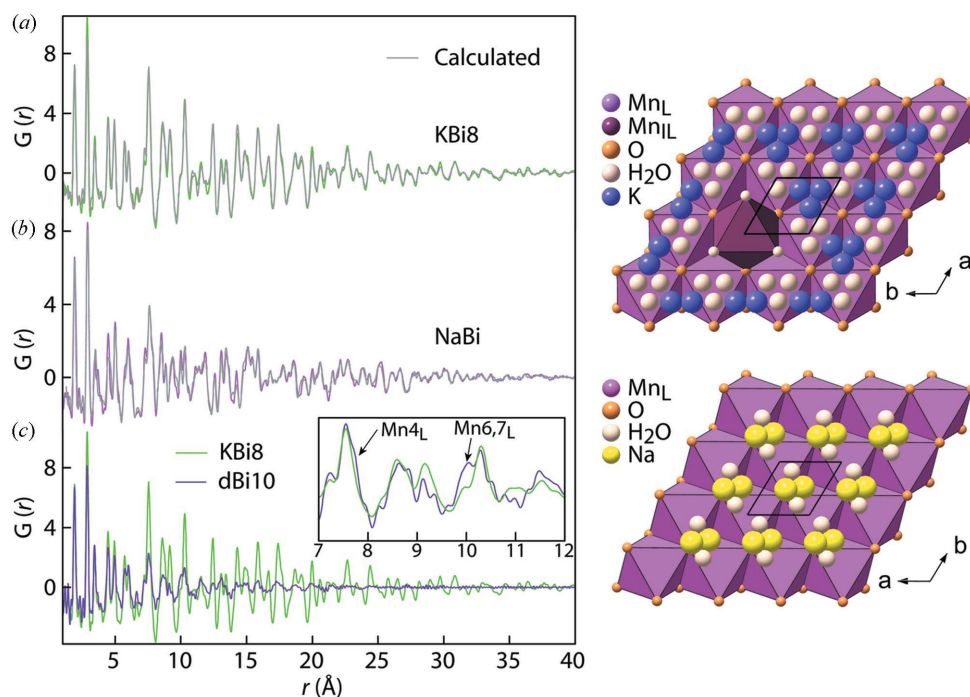

Figure 3
(*a*), (*b*) Experimental and calculated PDFs for the two crystalline phyllomanganate references KBi8 and NaBi shown on the right (fractional site occupancies have been omitted). (*c*) PDFs for crystalline KBi8 and nanocrystalline dBi10 showing the loss of structural coherence above 7–8 Å in dBi10 caused by turbostratic disorder. The expanded 7–12 Å region in the inset shows that dBi10 has a wider distribution of $Mn\cdots Mn4_L$ and $Mn\cdots Mn6,7_L$ distances. The amplitude for the PDF of KBi8 was scaled in the inset to aid comparison with dBi10.

Alain Manceau *et al.* · Order of phyllomanganate nanoparticles

research papers

(Waasmaier & Kirfel, 1995) and omitting anomalous dispersion. Water molecules were approximated as O atoms. Since *CALCIPOW* does not allow a distribution of CSD size in the *ab* plane, a lognormal size distribution (σ_{CSD}) was simulated by integrating scaled versions of the shape function $T(U)$ (Drits & Tchoubar, 1990) over the distribution (supplementary materials,[1] note S1). Similarly, *CALCIPOW* does not natively contain strain factors to model the bending of the nanosheets. Strain causes the crystals to diffract at high q as if they were smaller, since the coherent part shrinks with increasing q. Reflections from the Bragg lines at the edges of a particle go out of phase with those at the center, and this happens when the displacement, with respect to the reference structure, hits about half a d spacing. Thus, when d gets small, the apparent CSD size diminishes. A physically realistic form for this effect is

$$CSD[hkl]^{-2} = CSD[real]^{-2}[1 + \delta(q/q_{10})^2], \qquad (1)$$

where CSD[real] is the actual size of the crystallite, δ is a dimensionless parameter describing strain and q_{10} is the scattering vector for the first in-plane reflection. This form was chosen so that at high q the width of a reflection is proportional to δq, as expected from strain broadening. Different CSD sizes for different reflections were implemented by generating sets of input files for each set of reflections having a common $|q|$ and adding up the resulting $I(q)$ outputs, when δ is nonzero. All CSD[hkl] values were assumed to have the same lognormal distribution. Therefore, including strain effect in the modeling introduced only one new parameter. Finally, the simulated data were fitted to the measured, allowing an estimation of the background as follows:

$$I_{meas}(q) = aI_{calc}(q) + b_0/q + b_1 + b_2q, \qquad (2)$$

with a, b_0, b_1, b_2 being fitting parameters.

2.5. Debye equation analysis

The DE procedure starts with defining a structure for a single layer, calculating the powder-average diffraction from that layer and then fitting to the data.

2.5.1. Defining the structure. The structure is basically an MnO_2 layer restricted to a given size, but with modifications and crystal chemical constraints (supplementary materials, note S2). These modifications include (1) the occurrence of layer vacancies, under the constraint that no two vacancies can be neighbors, (2) the attachment of Mn_{IL} atoms and their coordinated water molecules above or below empty Mn_L sites, (3) the addition of mid-interlayer Na and water molecules, with the requirement that these atoms do not approach each other too closely, and (4) the bending of the layer around a spherical or cylindrical mandrel such that the neutral plane is the layer plane $z = 0$. This bending was parameterized by the reciprocal bending radii in the **x** and **y** directions. The structural parameters are, therefore, the site occupancies and

position parameters, the inverse bending radii (in this study, kept the same for all crystals), the layer b lattice parameter, and the displacement parameters of the atoms, which are assumed to be the same as in the Bragg-rod approach and which have been previously used for modeling diffraction data for these materials (Villalobos *et al.*, 2006; Grangeon *et al.*, 2008, 2009, 2012).

Because the structure has randomness, it is necessary to simulate not just one but many structures, averaging their scattering (Oddershede *et al.*, 2008). Polydispersity may be modeled by allowing the layer size to be a random variable, with a lognormal distribution. Thus, each modeled particle may have a different size and distribution of vacancies. Polydispersity becomes important when it is small, because the rare large particles can contribute disproportionately to the diffraction. As a result it takes many particles to get a good statistical average. The amount of time and memory required to perform the calculation also depends strongly on the size of the largest particle considered.

2.5.2. Calculation. Like Cervellino's group, we used the following Debye equation (Cervellino *et al.*, 2010; Cernuto *et al.*, 2011):

$$\begin{aligned} I(q) &= \frac{1}{N_L} \sum_{i=1}^{N_L} \sum_{j=1}^{N_L} f_i f_j^* \mathrm{sinc}(q|\mathbf{r}_i - \mathbf{r}_j|) \\ &= \frac{1}{N_L} \left[\sum_{i=1}^{N_L} |f_i|^2 + 2 \sum_{i=2}^{N_L} \sum_{j=1}^{i-1} \mathrm{Re}(f_i f_j^*) \frac{\sin(q|\mathbf{r}_i - \mathbf{r}_j|)}{q|\mathbf{r}_i - \mathbf{r}_j|} \right], \end{aligned}$$

$$(3)$$

in which $\mathbf{r}_i$ is the position of the ith atom, q the scattering vector magnitude, f_i its scattering factor and N_L the total number of atoms.

Atomic motion or displacement from nominal sites may be treated in two ways. One is to use the $\exp(-U_i q^2)$ Debye–Waller term, where U_i is the displacement parameter for the displacement of atom i as customarily defined in diffraction (Trueblood *et al.*, 1996) and used in the Bragg-rod and PDF simulations. The obvious way to do this is just to multiply all atomic scattering factors $|f_i|^2$ by the appropriate Debye–Waller factors, just as one would do in a calculation of intensities for a crystal. However, if we assume atomic motions to be uncorrelated and isotropic, the statistical average over all Gaussian distributions of atomic positions yields

$$\begin{aligned} I = \frac{1}{N_L} &\left\{ \sum_{i=1}^{N_L} |f_i|^2 + 2 \sum_{i=2}^{N_L} \sum_{j=1}^{i-1} \mathrm{Re}(f_i f_j^*) \frac{\sin(q|\mathbf{r}_i - \mathbf{r}_j|)}{q|\mathbf{r}_i - \mathbf{r}_j|} \right. \\ &\left. \times \exp[-(U_i + U_j)q^2/2] \right\}. \end{aligned} \qquad (4)$$

Note that the first term is not a representation of the Debye–Waller factor. The difference between the form used here and one in which the first $|f_i|^2$ term is multiplied by the exponential is referred to as thermal diffuse scattering. Uncorrelated motions may also be simulated more explicitly by applying random displacements to each atom, with mean-square displacements in each direction given by $\langle u_{x,i}^2 \rangle = U_i$. Tests

showed that the two methods yield similar results, as expected. Disorder-induced uncorrelated displacement was simulated with the Debye–Waller modified Debye equation (4) instead of explicit random displacements in order to avoid the statistical 'noise' that random atomic displacements would produce. In principle, correlated motions and motions whose amplitudes depend on direction and environment may be easiest to handle using explicit displacements. A fitted background of the same form as in the Bragg-rod method was added. However, its shape is different because the DE method includes the '000' reflection from the layer as a whole, in contrast to the Bragg-rod formalism.

For a given set of parameters, from 100 to 1000 structures were included in the analysis and the resulting r_{ij} distance histograms and $I(q)$ averaged. As mentioned above, if we want to include polydispersity, we do so by having each calculated diffraction pattern computed from a structure of size chosen from the specified distribution of sizes. Each structure tried corresponds to a unique arrangement of atoms, so there is no way to produce an 'average' structure. Instead, we save the coordinates of the structure that produces the best fit to the diffraction data of all those tested. Details can be found in the supplementary materials, note S2.
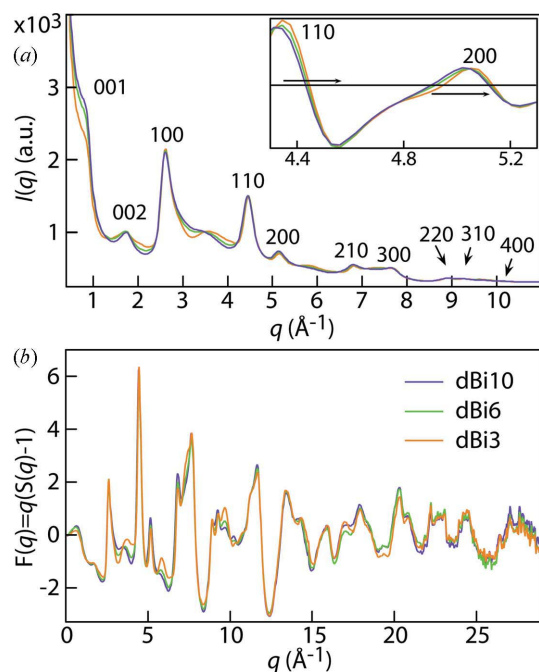
Table 2
Unit-cell and atom-independent parameters from the PDF analysis and XRD when available.

The domain size was modeled with a sphere. q_{damp} and q_{broad} are instrumental resolution parameters.

	KBi8			NaBi					
	XRD	Model 1	Model 2	XRD	Model 1	Model 2	dBi10	dBi6	dBi3
Space group	$P6_3/mmc$			$P\bar{1}$			$P\bar{3}$	$P\bar{3}$	$P\bar{3}$
a (Å)	2.845	2.85†	2.85†	2.951	2.940	2.939	7.564 (6)†	7.560 (4)†	7.554 (3)†
b (Å)	2.845	2.85†	2.85†	2.955	2.962	2.966	7.564 (6)†	7.560 (4)†	7.554 (3)†
c (Å)	14.23	14.21	14.21	7.33	7.33	7.33	7.20‡	7.20‡	7.20‡
α (°)	90	90‡	90‡	78.7	78.7	78.7	90	90	90
β (°)	90	90‡	90‡	101.8	101.8	101.7	90	90	90
γ (°)	120	120‡	120‡	122.3	122.2	122.2	120	120	120
Scale		1.10	1.09		0.99	1.04	1.09	1.03	0.97
q_{damp}		0.04‡	0.045‡		0.045‡	0.045‡	0.0‡	0.0‡	0.0‡
q_{broad}		0.040	0.041		0.002	0.001	0.0‡	0.0‡	0.0‡
δ_2		2.44	2.46		3.2	3.4	2.8	3.1	2.8
Diameter (Å)		68	70		68	62	17	16	16
Mn_L occupancy		0.92	0.92				0.87	0.84	0.83
Mn_{IL} occupancy		0.03	0.03				0.08	0.15	0.21
R_w (%)		18.7	19.0		30.9	30.4	16.5	20.2	18.6

† Kept equal. ‡ Fixed.

3. Results and discussion

The q-space structure functions of the three dBi samples are shown in Fig. 4(a). Structural disorder suppresses rapidly the sine-wave HEXS features at increasing q, resulting in very weak Bragg peaks at higher diffraction angles. The overall drop-off in intensity follows $|f_i|^2$ with very weak apparent scattering features in the $11 \leq q \leq 29$ Å⁻¹ region. However, when the data are divided by $|f_i|^2$ and multiplied by q to calculate the reduced structure functions $F(q) = q[\mathrm{S}(q) - 1]$ (Egami & Billinge, 2003; Billinge & Kanatzidis, 2004), large amounts of diffuse scattering become apparent in this region (Fig. 4b). Diffuse scattering is also present at low q ($< {\sim}5$ Å⁻¹) between poorly defined Bragg diffraction peaks, but is relatively more pronounced at high q ($> {\sim}10$ Å⁻¹). This signal contains information on the local structure, which is revealed in the low-r region ($< {\sim}7$ Å) of the Fourier transform. We first examine by PDF analysis the diffuse scattering signal, which from its pronounced intensity reflects the presence of well defined, yet aperiodic, coordination spheres at the nanometre scale. We next analyze the HEXS profiles, first with the Bragg-rod method in the $0.4 \leq q \leq 11.0$ Å⁻¹ interval, which includes the two basal 001 and 002 reflections and the hk bands, then with the Debye method in the $2.0 \leq q \leq 11.0$ Å⁻¹ interval, which excludes basal reflections. The first method gives the average crystallographic structure in the layer plane (hk bands) and perpendicularly (00l reflections), and shows evidence for significant long-range structural distortions of the layer plane that are not captured realistically by this approach.

Figure 4
(a) Raw intensity data of δ-MnO₂ equilibrated at pH 10 (dBi10), 6 (dBi6) and 3 (dBi3). Broad Bragg peaks are observed up to the maximal q value of 11 Å⁻¹. Intensity at higher q is suppressed by the rapid fall off of the composition-averaged scattering factor $\langle|f_i|^2\rangle$ with increasing diffraction angle. The inset shows on an expanded scale the reduction of the lattice a and b parameters at acidic pH as a result of the increase of layer vacancies. (b) The reduced structure function $F(q)$ from the same data after making corrections for experimental effects (Wagner, 1978) and dividing the scattered intensity by $\langle|f_i|^2\rangle$ and multiplying it by q to amplify the diffuse intensity at high q.

Alain Manceau *et al.* · Order of phyllomanganate nanoparticles

A more concise description of the long-range microstructure is obtained by bending spherically or cylindrically the layer plane and calculating its X-ray scattering with the second method.

3.1. PDFs

3.1.1. Crystalline phyllomanganates. Lattice constants and all independent atomic coordinates allowed by space-group symmetries were set initially to their crystallographic values and subsequently refined. A total of 16 parameters were varied for KBi8 and 24 for NaBi (Table 2, and Table S1 in supplementary materials). The first fit returned an R_w value of 18.7% and the second 30.9% (Figs. 3a and 3b). The higher R_w value for NaBi reflects greater uncertainty in its structure (lower symmetry) and higher structural heterogeneity of the constitutive crystallites. The refined lattice constants and

Figure 5
(a) Experimental PDFs for δ-MnO$_2$ synthesized as a function of pH, showing the reverse variation of the Mn$\cdots$Mn$_L$ and Mn$\cdots$Mn$_{IL}$ pairs as a result of the layer-to-interlayer migration of Mn$_L$ at acidic pH. The closest approach of any two Mn$_{IL}$ atoms is 7.2 Å. This occurs when the two Mn atoms are located on opposite sides of the layer and positioned on a diagonal across an intervening layer Mn (Mn$_{IL\uparrow}\cdots$Mn$_L\cdots$Mn$_{IL\downarrow}$ configuration), as illustrated in Fig. 6(c). (b) Best-fit PDF profiles up to 8.5 Å calculated for a model containing 17% vacancies (Fig. 6c). This model reproduces the pH variation of the Mn$\cdots$Mn pairs, except for the Mn$_L\cdots$Mn3$_{IL}$ correlation, which is overestimated. (c)–(e) Best-fit PDF profiles up to 7 Å calculated for a chalcophanite model (Fig. 6d). This model reproduces the short-range relaxation of the Mn$\cdots$Mn and Mn—O distances around vacancies.

coordinates for the layer species are close to the starting model, whereas the positions for Na/K and H$_2$O differ quite substantially, from about $y(\text{H}_2\text{O})_{\text{KBi8}} = 0.024$ to as much as $x(\text{H}_2\text{O})_{\text{NaBi}} = 0.13$.

The reliability of the refined interlayer positions was tested next by fixing their positions to the crystallographic values (Model 2, Table 2). This led to a reduction in the total number of parameters fitted from 16 to 14 (KBi8) and from 24 to 18 (NaBi), yet without affecting R_w, which remained invariant: 19.0 versus 18.7% previously (KBi8), and 30.4 versus 30.9% (NaBi). From this result we conclude that the PDF data do not contain enough information to precisely determine the positions of light and weakly bound Na/K and H$_2$O interlayer species (Gateshki et al., 2004; Zhu et al., 2012). Hence, an absence of parameter correlations (<0.8), as reported by PDFgui, does not mean that the refined values are precise. Because the Na$^+$/K$^+$ ions balance the negative charge of the layer, their occupancies may be linked to that of Mn$_L$ (Zhu et al., 2012), but this constraint is not fully justified when the layer contains substitutions of Mn^{3+} for Mn^{4+} in addition to vacancies, or when the interlayer contains H$^+$ in addition to Na$^+$/K$^+$ (Villalobos et al., 2006; Lanson et al., 2000).

The $z(\text{Mn}_{IL})$ fractional coordinate in KBi8 is about the same whether determined with XRD ($z = 0.150$) or PDF analysis ($z = 0.150$–0.154). However, the PDF method returns an Mn$_{IL}$ occupancy of only 0.03 per layer octahedron, for a theoretical value of 0.08. Fixing the occupancy to 0.08 increased R_w from 19.0 to 20.2, a significant change. Therefore, the refined value of 0.03 is probably precise, but some uncertainty remains on the accuracy of the PDF estimation. The actual fraction of Mn$_{IL}$ may be lower than estimated, because this sample was synthesized more than ten years ago (Gaillot et al., 2003). Interlayer Mn is considered to be trivalent. If for some reason it oxidized with time, as suggested by XANES spectroscopy (Manceau et al., 2012), then Mn^{4+} would probably have migrated into vacancies, thus decreasing the effective amount of Mn$_{IL}$.

3.1.2. Nanocystalline phyllomanganates. The two dimensionality of the δ-MnO$_2$ nanosheets and their limited structural coherence within the ab plane is clearly seen in their PDFs (Fig. 3c). The PDF peaks of the dBi samples have similar intensities to those of KBi8 out to distances of 7.2 Å and are abruptly lowered above this value, decaying progressively toward zero at $r = 20$ Å. The loss of peak intensity occurs at a distance equal to the c lattice parameter and results from the smearing of the layer–layer interactions caused by the lack of layer registry in this direction. The loss of structural coherence along the δ-MnO$_2$ sheets to distances of about 20 Å arises from the termination of sheet fragments, the small curvature of the sheets and the distribution of curvatures in the sample (Fig. 2). Thus, the fall-off in peak intensity beyond 7.2 Å has several origins which, collectively, are too complex to model. Nevertheless, the low-r interval is already rich in information and provides direct insight into the short-range structure of dBi and its modification with pH.

Two types of peaks are observed in the PDFs of dBi: those corresponding to Mn—O correlations, which are essentially
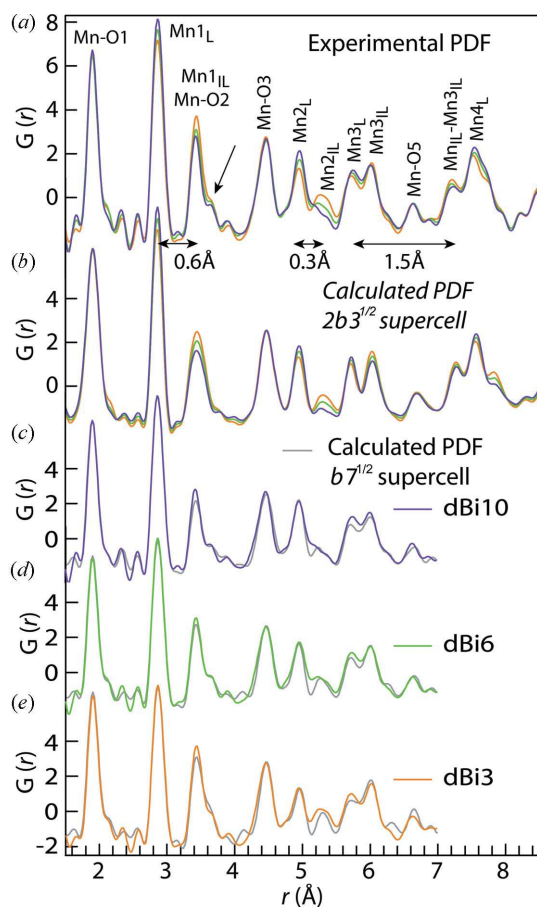
independent of pH, and those corresponding predominantly to Mn···Mn correlations, which evolve with changing pH (Fig. 5a). All the Mn_L···Mn_L correlations decrease with decreasing pH, and all the Mn_L···Mn_{IL} correlations increase when the pH decreases. The Mn_L···Mn_L and Mn_L···Mn_{IL} peaks alternate with a distance separation of about 0.6, 0.3 and 1.5 Å. The regular negative and positive alternation of Mn_L peak intensities with changing pH, and the contrasting irregularity of their distance separation, indicate significant short-range order of the Mn_L and Mn_{IL} atoms in the structure. The peculiarity of the PDF correlations can be understood with a honeycomb hexagonal pattern of unit-cell b dimension equal to $d(Mn_L···Mn1_L) = 2.86$ Å (Fig. 6). The decrease of the Mn_L···Mn_L correlations with decreasing pH at about 2.86, 4.95, 5.72 and 7.57 Å corresponds to the loss of Mn neighbors in the first four layer cationic shells at $d = b$, $3^{1/2}b$, $2b$ and $7^{1/2}b$. We cannot conclude from this result if the vacancies are ordered in the layer, as exemplified in Figs. 6(a)–6(c) with three models featuring 17, 25 and 33% vacancy ordering. Each of them is consistent, at least qualitatively, with the experimental variation of the Mn_L···Mn_L pairs with pH. As will be shown below, the average distribution of vacancies and interlayer manganese can be obtained from the analysis of the Mn_L···Mn_{IL} and Mn_{IL}···Mn_{IL} pairs.

In phyllomanganates, when an Mn atom leaves the layer and creates a vacancy, it fills one of the two symmetry-equivalent interlayer sites located immediately above and below the vacancy (Drits, Silvester *et al.*, 1997; Silvester *et al.*, 1997). In this interlayer site, the Mn_{IL} atom is bonded to the layer through three O atoms in a triple-corner-sharing (TCS) arrangement with the nearest layer octahedra (Fig. 1). In KBi8, the Mn_L···$Mn1_{IL}$ TCS distance is 3.54 Å. If we take this value and $b = 2.86$ Å and invoke geometric considerations, the second and third Mn_L···Mn_{IL} correlations are at 5.40 and 6.13 Å. The Mn···$Mn2_{IL}$ correlation is observed experimentally at 5.20–5.40 Å and Mn···$Mn3_{IL}$ is absent. The absence also of $Mn1_{IL}$···$Mn1_{IL}$ correlation at about 4.25 Å prohibits the existence of TCS pairs across vacancies ($Mn1_{IL↑}$···$Mn1_{IL↓}$ configuration), which therefore are singly capped (Fig. 1). A plausible short-range structure model can be deduced from these observations as follows. The layer has less than 33% vacancies on average, otherwise the Mn···$Mn2_{IL}$ correlation would be absent or weak and the Mn···$Mn3_{IL}$ correlation would be observed at low pH (Fig. 6a). Also, above 33% some vacancies are adjacent, which is structurally unrealistic. An average of 25% vacancies yields (1) the desired correlation at ∼7.2 Å, which occurs when two Mn_{IL} atoms from successive interlayers are positioned on a diagonal across an intervening layer Mn, and (2) no Mn···$Mn3_{IL}$. The Mn sequence corresponding to the ∼7.2 Å correlation can be depicted as $Mn_{IL↑}$···$Mn1_L$···$Mn3_{IL↓}$. However, careful inspection of the PDFs suggests that the ∼6.13 Å peak indicative of Mn···$Mn3_{IL}$ pairs may not be totally invariant with pH, increasing slightly at pH 3. This observation can be accounted for by lowering the vacancy density, as shown for example with the third hexagonal honeycomb pattern featuring 17% vacancies. Another distinguishing characteristic of the 17% vacancy-ordered model relative to the 25% version is the absence of $Mn_{IL↑}$···$Mn1_L$···$Mn3_{IL↑}$ sequences as every $Mn_{IL↑}$ is surrounded by three $Mn3_{IL↓}$, and *vice versa*. From 17% vacancies, $Mn_{IL↑}$···$Mn3_{IL↑}$ correlations appear in the interlayer, at the same distance as the Mn_L···$Mn3_L$ correlations. Hence, the $Mn_{IL↑}$···$Mn3_{IL↑}$ correlations should attenuate the decrease of the Mn_L···$Mn3_L$ correlation with pH. This finding seems to be supported by the data, which show that the Mn_L···$Mn2_L$ peak has a higher amplitude variation than does the Mn_L···$Mn3_L$ peak.

The hexagonal $2(3^{1/2})b$ supercell featuring 17% vacancies was fitted to the experimental PDFs and structure parameters, such as unit-cell constants, atomic coordinates, Mn_L and Mn_{IL} occupancies, and displacement parameters, and refined to obtain the best possible agreement between the calculated and experimental data. As can be seen in Fig. 5(b), this model reproduces well the variation with pH of the three PDFs, with the exception of the Mn_L···$Mn3_{IL}$ correlation and, to a lesser extent, the $Mn_{IL↑}$···$Mn3_{IL↓}$ correlation. The pH dependence of the first correlation is overestimated in the calculation, and that of the second underestimated. The opposite variation means that the density of vacancies is higher than 17% at pH 3, as discussed previously. The structure model also fails to reproduce the bimodal distribution of the Mn···$Mn1_{IL}$ [arrow in
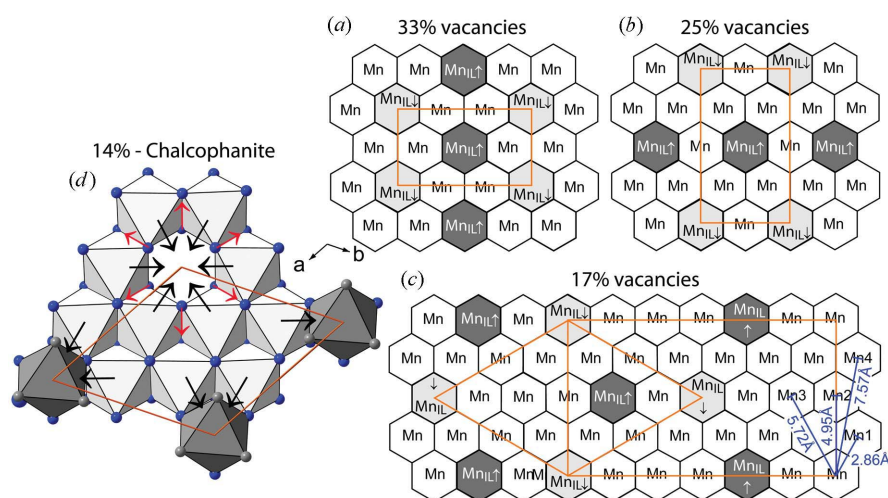
Figure 6
Layer structures considered as trial models in the short-range order determination of nanocrystalline δ-MnO$_2$. (a) $3^{1/2} × 3b$ C-centered orthogonal layer cell featuring 33% vacancies. (b) $2(3^{1/2}) × 2b$ C-centered orthogonal layer cell featuring 25% vacancies. (c) $2(3^{1/2}) × 6b$ C-centered orthogonal layer cell featuring 17% vacancies. The equivalent hexagonal $2(3^{1/2})b$ supercell is also represented. (d) Top view of the MnO$_2$ layer for chalcophanite containing 14% vacancies. Arrows indicate the directions of the Mn (black) and O (red) displacements upon structural relaxation induced by Mn vacancies. The gray octahedra are interlayer Mn (a)–(c) or Zn (d).

 Alain Manceau et al. · Order of phyllomanganate nanoparticles

Fig. 5(a)] and Mn$\cdots$Mn2_{IL} distances, and the large distribution of the Mn$\cdots$Mn2_L, Mn$\cdots$Mn3_L, Mn$\cdots$Mn4_L and Mn$\cdots$Mn$6,7_L$ distances featured by the width of the corresponding peaks [see *e.g.* inset in Fig. 3(c)]. The Mn$_L$ peak widths tend to decrease with decreasing pH, that is with the number of Mn atoms in the layer. These observations constitute strong support for a structural model that includes a local-scale distortion of the manganese layer, thus raising the need to consider another unit cell, one in which the Mn$_L$$\cdots$Mn$_L$ distances are unequal.

Quantum mechanical calculations, based on spin-polarized density functional theory (DFT), have shown that an Mn vacancy causes considerable local distortion of the octahedra near the vacancy site through lateral displacements of the neighboring Mn and O atoms but that average interatomic distances remain relatively unaffected (Kwon *et al.*, 2009a). Several trial displacements were tested on the 17% vacancy-ordered model, all featuring a relaxation of the Mn sites while retaining the hexagonal symmetry of the layer. Given notably the reduced *r*-fit interval, they all proved unsuccessful. The supercell introduces too many inequivalent sites, requiring more fitting parameters and introducing extraneous correlations. To cope with the relaxation of the Mn sites around a vacancy, it was necessary to take a smaller cell and refine the model against the experimental data while observing space-group constraints. A model based on the structure of chalcophanite (ZnMn$_3$O$_7\cdot$3H$_2$O) performed best. Its one-layer supercell can be represented with the $P\overline{3}$ space group (Fig. 6d). Its dimension is $7^{1/2}b$ with b = 2.847 Å, and it features six symmetry-equivalent Mn$_L$ sites and one vacancy doubly capped by Zn$_{IL}$, instead of Mn$_{IL}$ in δ-MnO$_2$. The density of vacancies (1/7 = 14%) is too low to model the Mn$_{IL\uparrow}$$\cdots$Mn$3_{IL\downarrow}$ correlation at 7.2 Å, but it adequately explains the PDF out to r = 7.0 Å (Figs. 5c–5e). The refined PDF parameters describing the short-range order of dBi with the chalcophanite model are listed in Tables 2 and S1, and structural formulae are given in Table 1. They were calculated on the basis of the Mn$_L$ and Mn$_{IL}$ site occupancies obtained through analysis of the PDF data (Table 2), Mn^{3+}/Mn^{4+} ratios as obtained by titration, Na/Mn ratios as obtained by chemical analysis, and H$_2$O content as derived from weight loss upon heating. These results are examined next.

In chalcophanite, the six Mn$_L$ atoms around a vacancy are displaced inward, toward the vacancy site, by 0.05 Å (2.81 Å) as compared to their positions in vacancy-free MnO$_2$ (d = 2.86 Å) (Post & Appleman, 1988). The Mn$_L$$\cdots$Mn$_L$ pairs that do not border the same vacancy are correspondingly lengthened by 0.04 Å [d(Mn$_L$$\cdots$Mn$1_L$) = 2.90 Å], thus preserving the hexagonal symmetry of the layer (Fig. 6d). At the same time, the O$_L$ atoms bonded to Zn$_{IL}$ and Mn$_L$ are displaced outward from the vacancy to compensate for the inward displacement of the Mn$_L$ atoms and to screen the local Mn$_L$ charge by shortening the length of the shared edge of the Mn octahedra delimiting the empty cavity (Manceau *et al.*, 2002; Kwon *et al.*, 2009b). The magnitude of the local distortion induced by vacancies is essentially comparable in δ-MnO$_2$ and chalcophanite. The as-refined dBi3 structure has

$\langle d(\text{Mn}\cdots\square)\rangle$ = 2.83 Å and $\langle d(\text{Mn}_L\cdots\text{Mn}1_L \text{ outer})\rangle$ = 2.90 Å, and $\langle d(\square\cdots\text{O})\rangle$ = 1.96 Å instead of 1.93 Å in an undistorted structure, leading to a decrease of the shared-edge length from 2.59 to 2.48 Å. One of the main differences between chalcophanite and δ-MnO$_2$ is in the variation of the Mn$_L$$\cdots$(Mn/Zn)$1_{IL}$ distances, which are equal to 3.48 and 3.50 Å in the crystalline phyllomanganate and between 3.40 and 3.62 Å in the nanocrystalline phyllomanganate. The larger distribution observed in dBi results, at least in part, from the Jahn–Teller distortion of the Mn^{3+} octahedra present in the interlayer. A signature of the strong local distortion of the nanocrystals caused by vacancies and Mn^{3+} octahedra is seen in the PDFs at r = 3.4–3.6 and 5.2–5.4 Å. As for the Mn$_{IL}$—O distances, the chalcophanite model has one important limitation. The three O$_L$ atoms bordering a vacancy, and the three water molecules in the interlayer, are symmetry equivalent and equidistant from Zn at 2.07 and 2.14 Å (Post & Appleman, 1988). This threefold symmetry imposed by the trigonal cell is an unsatisfactory approximation for a Jahn–Teller-distorted Mn^{3+} octahedron with four short Mn—O bonds at about 1.93 Å and two long bonds at about 2.22 Å (Armstrong & Bruce, 1996). Consequently, the modeled Mn$_{IL}$—O distances are less precise than the Mn$_L$$\cdots$Mn$_{IL}$ distances. This explains why the amplitude of the third PDF peak is imperfectly reproduced.

Lowering the pH from 10 first to 6 and then to 3 increases concomitantly the vacancies and Mn$_{IL}$ occupancies from 0.08 to 0.15 and to 0.21 per layer octahedron (Table 2). The density of vacancies at pH 3 is close to the highest values reported previously, namely 24% for Zn-sorbed dBi at pH 5 (Grangeon *et al.*, 2012) and 22% for a natural plant-root Zn/Ca-containing dBi (Lanson *et al.*, 2008). The low-pH structural transformation of δ-MnO$_2$, described herein for the first time, has a parallel in the case of monoclinic/triclinic Na birnessite (NaBi), which is stable at alkaline pH and transforms into hexagonal birnessite (HBi) at acidic pH by losing its sodium and expelling 6.7% of its layer manganese into the interlayer (Silvester *et al.*, 1997). The PDF b parameter of the unit cell is equal to 7.564 (6)/7$^{1/2}$ = 2.859 (2) Å at pH 10 and to 7.554 (3)/7$^{1/2}$ = 2.855 (1) Å at pH 3; it is therefore almost invariant with pH despite the two and a half times increase of the density of vacancies. The main reason is that the PDF directly measures the Mn$\cdots$Mn distances, not the lattice dimension, in contrast to the Bragg-rod method.

To summarize, PDF data have enabled us to describe the structural relaxation around Mn vacancies, and the coordination environment and distribution of Mn in the interlayer region out to distances of 7.2 Å, a difficult task for current experimental techniques. In comparison, X-ray absorption spectroscopy provides information over a more limited distance range, which in the case of δ-MnO$_2$ does not extend beyond the Mn$_L$$\cdots$Mn$1_{IL}$ pair at about 3.5 Å (Villalobos *et al.*, 2006). The short-range order revealed by the PDF is characterized by large-amplitude local fluctuations of the atoms away from their mean positions, as determined for instance by the Bragg-rod method. Vacancies, and to a lesser extent the Mn^{3+} cations in the layer and interlayer, move the Mn$_L$ and O$_L$ atoms laterally from their average positions, but also slightly

out of the (001) plane (Table S1), creating a small corrugation of the layer at the surface, as is often the case for systems in which there is lattice site disorder or vacancies. All these displacements lead to notable variability in the interatomic distances around the vacancy site. Part of this variability is caused by the displacement of the surface O-atom positions around a vacancy required to fit the coordination geometry of the interlayer cation (here Mn^{3+}). Therefore, the short-range layer structure described in this study is not static and should vary, for the same material, with the nature of the interlayer cation, as illustrated here with Mn^{3+} *versus* octahedral Zn^{2+}. This finding was also suggested from DFT calculations for Pb^{2+} and tetrahedral *versus* octahedral Zn^{2+} (Kwon *et al.*, 2009b, 2010). Our PDF analysis, in combination with chemistry, also reveals that proton sorption at low pH expels layer Mn, thus creating new vacancies. Similarly, Zn sorption on dBi was reported to expel 10% Mn_L at pH 5 and a Zn/Mn atomic ratio of 0.153 (Grangeon *et al.*, 2012).

The PDF provides insight into the partially ordered distribution of Mn_{IL} atoms at pH 3. The distance of closest approach of two vacancies, deduced from the shortest $Mn_{IL\uparrow}\cdots Mn3_{IL\downarrow}$ correlation at 7.2 Å, is equal to $2b$ (Figs. 6b and 6c). A vacancy-ordered supercell with $2b$ periodicity has 25% vacancies, close to the 21% in dBi3 and 24% in Zn-sorbed dBi (Grangeon *et al.*, 2012). From geometrical considerations, a supercell with more than 17% vacancies cannot be filled with $Mn_{IL\uparrow}\cdots Mn3_{IL\downarrow}$ pairs only. When the vacancy content approaches 25%, the $Mn_{IL\uparrow}\cdots Mn3_{IL\uparrow}$ pairs tend to align in rows, but this material is probably too defective to sustain long-range ordering, and $Mn_{IL}\cdots Mn_{IL}$ boundary disorder probably occurs. The increased ordering of Mn_{IL} placement at increasing surface loading is supported by previous electron diffraction investigations of hexagonal birnessite, which showed that Mn, Zn and Pb have an ordered or semi-ordered distribution within the interlayer, as revealed by the presence of supercell reflections (Drits, Silvester *et al.*, 1997; Drits *et al.*, 2002).

Lastly, there is no one-cell-fits-all solution to the PDF modeling of dBi, despite its well defined atomic structure on the nanometre length scale. Hence, our description of the layer structure out to 7.2 Å is inevitably incomplete and more insight into some complementary aspects of its short-range order could be gained from other modeling approaches. Reverse Monte Carlo simulation may be a useful aid to understanding (Tucker *et al.*, 2007; McGreevy, 2001). However, the number of bonding environments is likely to be too large to adjust the positions of atoms by this technique without introducing any other information supplied in the form of constraints, which would for instance replace the space-group symmetries of our PDF analysis.

3.2. Bragg rods

Faint and broad 001 and 002 reflections are observed at low q, consistent with the small number of layers in the nanoparticles seen by TEM (Fig. 4a). The positions of the maxima are at 7.6–7.8 and 3.7 Å and their sequence is irrational, a

result of the finite particle size in this direction (Reynolds, 1968; Villalobos *et al.*, 2006; Manceau *et al.*, 2007; Lanson *et al.*, 2008; Grangeon *et al.*, 2008, 2009, 2012). Computer calculations show that the particles have an average thickness of 14 Å and a layer-to-layer distance of 7.2 Å (Fig. 7). Thus, the volume-averaged nanoparticles contain about two layers, according to XRD, whereas this number is more likely around three based on TEM observations. This difference, reported previously for Zn-sorbed δ-MnO_2, at least in part arises from the bending of the layers, which makes the interlayer spacing non-uniform (Li *et al.*, 2007; Grangeon *et al.*, 2012). The fluctuation of the interlayer thickness increasingly broadens and weakens diffraction lines with q (defects of the 'second type') (Drits & Tchoubar, 1990; Guinier, 1994). This effect was not considered in the simulation but is observed on the 002 reflection. The widths, and hence positions, of the calculated 002 reflections are slightly off in the model prediction. The discrepancy appears more noticeable at pH 10 than at pH 3 because this effect is convoluted by the structure factor, which has a different profile in this region at the two pHs. A similar fluctuation dependence of the interlayer spacing of the XRD patterns has been described in the clay literature (Ferrage *et al.*, 2005; Lanson, 2011). Overall, the dBi particle thicknesses coincide with the c^* domain sizes reported for this type of material: 11–12 Å for Zn-sorbed δ-MnO_2 (Grangeon *et al.*, 2012), 10–15 Å for Ni-sorbed δ-MnO_2 (Grangeon *et al.*, 2008), 15–22 Å for fungal δ-MnO_2 (Grangeon *et al.*, 2010), 9 Å for grass-roots δ-MnO_2 (Lanson *et al.*, 2008), and 11.6 (5) Å (Bargar *et al.*, 2009) and 19–42 Å for δ-MnO_2 (Villalobos *et al.*, 2006). Calculation also predicts that the 003 reflection at $q =$
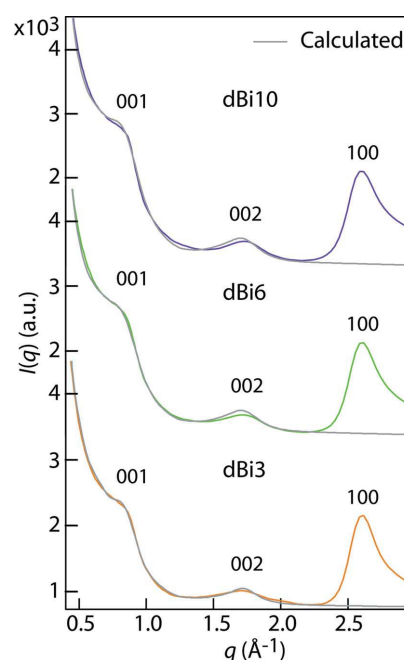
Figure 7
Modeling the basal XRD reflections shown in Fig. 4(a) using the Bragg-rod approach. The volume-averaged nanoparticles are modeled with a stack of δ-MnO_2 bi-layers with a layer-to-layer separation of 7.2 Å. The misfit of the 002 reflection comes from the non-uniformity of the interlayer spacing, as shown in Fig. 2.

Table 3
Atom-independent and unit-cell parameters from the Bragg-rod analysis.

	dBi10	dBi3
$a = b$ (Å)	2.853 (5)	2.833 (4)
c (Å)	7.20	7.20
CSD_{ab} (Å)†	58	58
$\sigma[\ln(CSD_{ab})]$‡	0.40	0.40
δ	0.20	0.20
CSD_{c*} (Å)	14	14
Mn_L occupancy	0.90	0.81
Mn_{IL} occupancy	0.08	0.21
$R_{wp} \times 10^3$	1.75	1.73
Normalized sum-squared error (NSS) $\times 10^3$	1.61	1.71

† Diameter of the disc-shaped domains. ‡ Lognormal distribution.

Table 4
Atom parameters from the Bragg-rod analysis (dBi10/dBi3).

The average layer structure may be represented with the $P\bar{3}m1$ space group without c translations.

	x	y	z	B (Å^2)†
Mn_L	0	0	0.0	0.5
O_L	2/3	1/3	0.129	1.0
Mn_{IL}	0	0	0.280	1.0
O_{IL}	1/3	2/3	0.480	2.0
Na‡	0.950§	0.475	1/2§	2.0
H_2O‡	0.400§	0.200	1/2§	2.0

† $B = 8\pi^2 U$, in Å^2. ‡ Equivalent positions: $(-x+y, -x, z)$ and $(-y, x-y, z)$. § Fixed to known positions (Grangeon *et al.*, 2008, 2012).

2.6 Å^{-1} should be extremely weak as observed in birnessite (Lanson, Drits, Feng & Manceau, 2002; Gaillot *et al.*, 2003). This is confirmed experimentally: otherwise the intensity maximum of the 10 reflection, also at $q = 2.6$ Å^{-1}, would vary with pH.

The lamellar character of the nanoparticles is well demonstrated by the asymmetric shape of the $q \geq 2.1$ Å^{-1} scattering bands on their high-angle side (Drits & Tchoubar, 1990). Abundant isosbestic points are observed up to $q = 11$ Å^{-1}, with the scattering intensity making a regular string-like pattern between them. The invariant scattering points parallel the clean evolution of the PDF peaks with pH (Fig. 5a) and confirm that the system appears pseudobinary. The dBi6 data between 2.1 and 11 Å^{-1} fit very nicely to a linear combination of those for dBi3 and dBi10 (coefficients 0.41 and 0.59, respectively). If we consider the structure of dBi6 to be 41% of the way from that of dBi10 to that of dBi3, we find the structural formula shown in Table 1 ('interpolated'), which agrees rather well with the refined formula for dBi6. The difference provides an error estimate of the refined stoichiometric values. The long tail of the strongest 10 band is noticeably modulated by the structure factor, and for this reason its line shape can be used for crystallographic structure identification of c^*-disordered layered materials (Drits *et al.*, 1984; Drits & Tchoubar, 1990; Villalobos *et al.*, 2006; Lanson *et al.*, 2008; Grangeon *et al.*, 2008, 2010, 2012; Lanson, 2011). Since the scattering intensity varies with pH to about 11 Å^{-1}, structural information also exists past the 10 band and can be recovered by extended modeling of the data.

All diffraction maxima at $q \geq 2.1$ Å^{-1} can be indexed with the $hk0$ indices from a hexagonal layer cell with $b = 2.853$ (5) Å at pH 10 and $b = 2.833$ (4) Å at pH 3 (Fig. 4a and Table 3). Unit-cell parameters were obtained from the simulations presented below, not directly from the positions of the hk maxima, because their positions are influenced by particle size and shape and stacking disorder. The $2.853 - 2.833 = 0.020$ Å reduction of b comes essentially from the increase of vacancies, because the PDF Mn$\cdots$Mn distances are nearly identical for the two pH samples, diminishing from 2.859 (2) Å to 2.855 (1) Å, and the amount of layer Mn^{3+} is apparently constant (Table 1). The close correspondence between PDF and Bragg b values at pH 10, where there are a minimum of

vacancies, attests to the reliability of the measurements. There is no evidence that the average layer symmetry deviates from hexagonal symmetry: a situation observed when the layer contains more than about 25% Mn^{3+} atoms ordered in rows with their long Mn^{3+}—O bonds all oriented in the same direction (Drits, Silvester *et al.*, 1997; Lanson, Drits, Feng & Manceau, 2002; Gaillot *et al.*, 2004, 2007; Chu *et al.*, 2011). Besides, the crystals are small, so if there is some tiny distortion of the average cell, the displacement of atoms from a 'best-fit' hexagonal position will be very small.

Neither the chalcophanite nor the 17% vacancy-ordered models could be used to fit to $q \geq 2.1$ Å^{-1} data within the Bragg-rod formalism because the long-range ordering of Mn$_{IL}$ and vacancies would result in superstructure reflections that are not observed experimentally. In the Bragg-rod approach, the basic units are sites with fractional occupancies and atom coordinates defined in a one-layer unit cell of hexagonal symmetry. Therefore, Mn$_{IL}$ and vacancies are treated as fractional. Within this formalism it is not possible to exclude specific short-range configurations based on crystal-chemical considerations, such as an Mn$_{IL}$ cation sitting above an occupied Mn$_L$ site and two neighboring vacancies. Compliance with fundamental crystal-chemical rules is ensured by verifying that fractional occupancies are not structurally unrealistic.

Best-model calculations are shown in Fig. 8 for dBi10 and dBi3, together with the effect of the CSD_{ab} distribution (σ_{CSD}) and microstrain (δ) parameters on the quality of the data modeling. The level of agreement between experiment and theory is fairly good, and the optimal parameter values are in close agreement with previous results on similar material (Tables 3 and 4) (Grangeon *et al.*, 2008, 2012). Comparison of layer and interlayer Mn occupancies derived from the Bragg-rod and PDF simulations shows that the two techniques yield similar results. In particular, both methods indicate that lowering the pH decreases the Mn$_L$ occupancy from 0.87–0.90 to 0.81–0.83 and consistently increases the Mn$_{IL}$ occupancy from 0.08 to 0.21. Excluding Na and water molecules from the dBi10 simulation modifies significantly the lineshape of the long 10 tail, confirming the sensitivity of this scattering region to light interlayer species, in contrast to the PDF method (Fig. 8b). The modeled nanoparticles have a CSD_{ab} diameter

of 58 Å with a $\sigma(\ln CSD)$ distribution of 0.4, which corresponds to an FWHM variation from 36 to 93 Å. CSD_{ab} values of 50–60 Å were reported previously for δ-MnO_2 synthesized under the same conditions (Villalobos *et al.*, 2006; Grangeon *et al.*, 2008, 2012). The model dependencies of σ_{CSD} and δ are shown in Figs. 8(*c*)–8(*e*) for dBi10. When $\sigma_{CSD} = \delta = 0$, the shape of the first *hk* band can be adjusted with the average CSD size, but the model completely fails at higher *q*. The model performs better when $\sigma_{CSD} \neq 0$, but still cannot be refined to reproduce the peak widths, even from the second band. A much better agreement with the data is obtained when the CSD size is varied with *q*, indicating that size broadening is
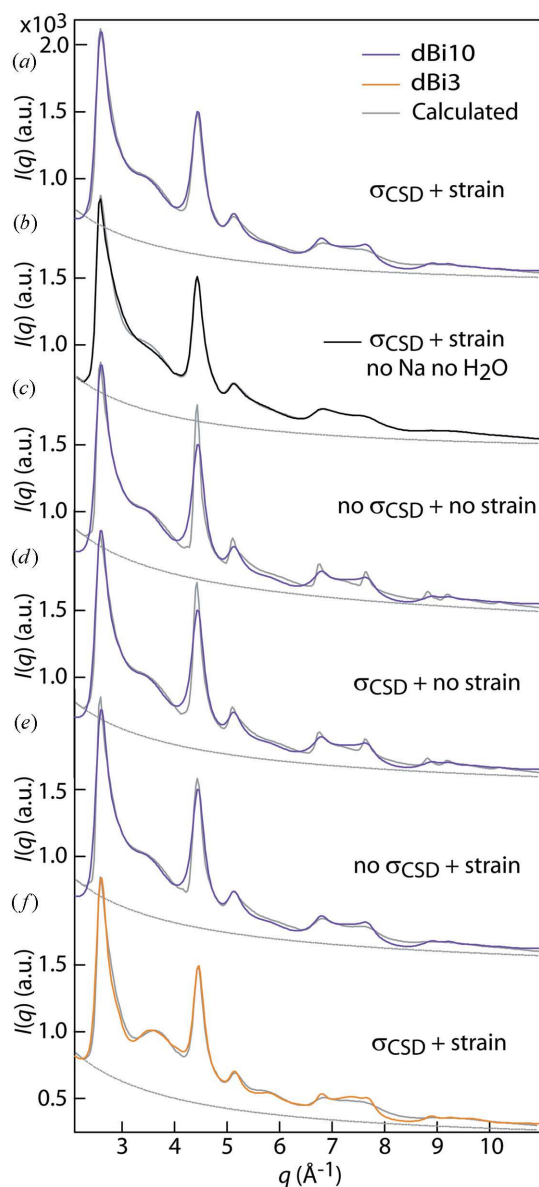
relatively negligible in comparison with microstrain widening at high *q*. However, both effects are needed to reproduce the lengthened left tail of the 11 band and hence its intensity relative to that of the 10 band. The effectiveness of the δ parameter to account for strain-widening effects is demonstrated in the 6.5–7.5 Å^{-1} region with the replication of the sawtooth shape of the overlapping 21 and 30 bands. The good agreement between experiment and theory demonstrates that the parametrization of the strain effect based on equation (1) is actually physically realistic, even though it cannot be interpreted in terms of a structural model. This interpretation will be realized below using the Debye method. In contrast to δ, a lognormal distribution of the CSD size for two-dimensional nanoparticles is a structurally meaningful quantity and the most realistic approximation for modeling their real distribution in size (Drits, Srodon & Eberl, 1997).

To summarize, the Bragg-rod simulation provides four complementary structural insights: (1) the volume-averaged nanocrystallite thickness as opposed to the area-averaged

Figure 8
Modeling of the *hk* XRD bands shown in Fig. 4(*a*) using the Bragg-rod method. (*a*) Best simulation obtained for δ-MnO_2 at pH 10 (dBi10). Sensitivity of the calculation to Na and nonbonded water molecules (*b*), to size distribution and strain (*c*), to strain (*d*), and to size distribution (*e*). (*f*) Best simulation obtained for δ-MnO_2 at pH 3 (dBi3). In (*b*) the sensitivity to Na and H_2O is illustrated (black line) by subtracting their contribution from the best-fit simulation shown in (*a*) (gray line).
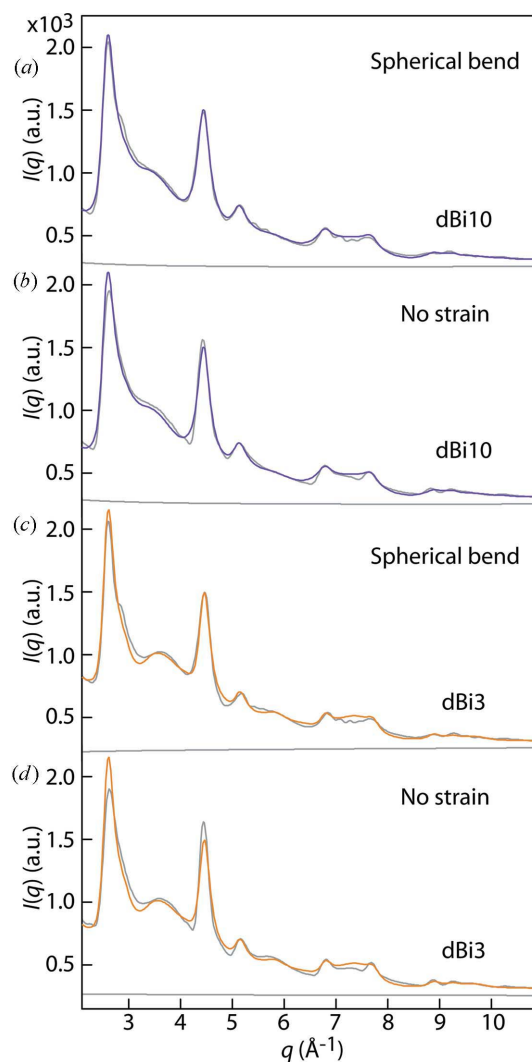

Figure 9
Best fits of the *hk* XRD bands for dBi10 and dBi3 using the DE method with and without strain.

Table 5
Parameters from DE analysis.

The mean nearest-neighbor Mn$\cdots$Mn distance of the average structure, $\langle R_{\mathrm{Mn}\cdots\mathrm{Mn}}\rangle$, equals b in the no-strain case. Errors were estimated by allowing b and strain to vary and looking for the limits over which the NSS increased by 10%.

	dBi10			dBi3		
	Spherical	Cylindrical	No strain	Spherical	Cylindrical	No strain
$a = b$ (Å)	2.908 (4)	2.870	2.853	2.881 (4)	2.846	2.833
$\langle R_{\mathrm{Mn}\cdots\mathrm{Mn}}\rangle$ (Å)	2.874 (3)	2.874	2.853	2.855 (2)	2.851	2.833
$\sigma^2_{\mathrm{Mn}\cdots\mathrm{Mn}} \times 10^{-4}$ (Å^2)†	15	0	0	10	0	0
CSD$_{ab}$ (Å)‡	39	38	28	43	44	33
Mn$_L$ occupancy	0.90	0.90	0.90	0.81	0.81	0.81
Mn$_{IL}$ occupancy	0.08	0.08	0.08	0.21	0.21	0.21
Bend radius (Å)	34 (7)	23	–	42 (5)	26	–
NSS $\times 10^3$	1.354	1.345	2.81	1.95	2.29	4.25

† Variance of nearest-neighbor Mn$\cdots$Mn distance distribution. ‡ No distribution assumed.

thickness obtained by TEM, (2) the mean unit-cell dimension, which in combination with the chemistry yields information about the fraction of vacancies and layer Mn^{3+}, (3) the lognormal distribution of the nanocrystallites within the *ab* plane, and (4) the apparent microstructure. While Bragg-rod simulation has a number of positive attributes, this approach alone can unambiguously determine with good accuracy only an apparent microstructure from a simplified analytical model. Below we show how the flexibility of the Debye formalism approach makes the implementation of structurally realistic strain models simple in the Debye equation.

3.3. Debye equation

While the Bragg-rod simulations gave considerable physical insight, they could not capture the effects of strain in a realistic way. The effect of strain is shown in Fig. 9 and the relevant structural parameters are provided in Table 5. The layers, assuming a spherical bend, have a volume-averaged apparent bend radius of 30–40 Å, consistent with TEM measurements (Fig. 2). The data from the pH 10 sample fit slightly better if we assume a cylindrical bend (axis along the chain direction; Li & Wu, 2009), for which the radius is about 23 Å (Fig. 1). For the pH 3 sample, the spherical bend fits better than the cylindrical bend. Spherical bending contributes a bump at 2.6 Å^{-1}, as seen in Fig. 9. A cylindrical bend moves this bump to 2.9 Å^{-1}. It is likely that a distribution of bend shapes and radii would blur out the bump, bringing the simulation into closer agreement with experiment. No curvature distribution (*i.e.* non-uniform strain) was considered, because HEXS data cannot support a more complex model and still achieve stable solutions. For the strained layer, the apparent lattice parameter is higher than for the unstrained case or the Bragg-rod-optimized structure; however, the Mn$_L\cdots$Mn$_L$ distance is comparable.

As seen in Figs. 6(*b*) and 6(*c*), the pH 3 sample has short-range ordering of the vacancy/Mn$_{IL}$ pairs as a result of their mutual repulsion. This effect is less prominent for the pH 10 sample because there are fewer vacancies at this pH (Fig. 1). On the basis of PDF results, Mn$_{IL\uparrow}\cdots$Mn$_{IL\downarrow}$ pairs cannot be

closer than 7.2 Å, which excludes the presence of nearest Mn$_{IL\uparrow}\cdots$Mn2$_{IL\downarrow}$ pairs at 6.3 Å [b = 2.833 (4) Å]. Structure models for dBi10 with this constraint enforced give almost identical DE results to the no-exclusion models because there are few Mn$_{IL}$ atoms at this pH and the data analysis, carried out in reciprocal space, lacks the sensitivity needed to characterize nonperiodic short-range ordering. It proved impossible to enforce the exclusion of Mn$_{IL\uparrow}\cdots$Mn2$_{IL\downarrow}$ pairs at 6.3 Å in the case of dBi3 because, despite 150 000 attempts, no randomly generated structure, as described in note S2 of the supplementary materials, satisfied this condition. At high density of Mn$_{IL}$, reverse Monte Carlo simulation may be more effective because more structurally acceptable configurations can be produced by swapping atomic pairs during the minimization procedure (Tucker *et al.*, 2007). In contrast to dBi3, it took an average of 17 tries to come up with a dBi10 structure that excludes the Mn$_{IL\uparrow}\cdots$Mn2$_{IL\downarrow}$ pairs. In both cases, each structure tested already obeyed the rules against double-capped and nearest-neighbor vacancies. Perhaps the real system finds it as difficult to reach an appropriate semi-ordered structure as our program does, because the lower the pH, the longer it takes to equilibrate dBi.

4. Concluding remarks

Extensive modeling of the HEXS data for turbostratic δ-MnO$_2$ nanosheets, complemented by high-resolution TEM to image their morphological microstructure, resulted in a fairly complete understanding of the local and long-range structure of this environmentally and technologically important material. It was found that the local atomic structure deviates significantly from the crystallographic average structure and is accurately revealed by analyzing atom correlations from the PDF. The local structure out to distances of 7.0 Å can be described rather well by a two-dimensional supercell and a small number of parameters. However, the long-range structure cannot be described rigorously by means of a unit cell repeated in three-dimensional space and ADPs as it is only coherent in the *ab* plane. This incorrect approximation led to previous conclusions that biogenic MnO$_x$ nanosheets have a todorokite-type three-dimensional tunnel structure (Petkov, Ren *et al.*, 2009; Grangeon *et al.*, 2010).

A further limitation of the PDF approach is its lack of sensitivity to the positions of interlayer species with low atomic numbers (Na, K, H$_2$O), as reported previously for this type of material (Zhu *et al.*, 2012) and similarly for SO$_4$ in tunnel-structure Fe oxyhydroxide (Fernandez-Martinez *et al.*, 2010). An illustration of the risk in trying to fit the whole PDF of Mn nanosheets with a defect-free crystal model and nonphysical ADPs is provided in Fig. 10 with the example of acid birnessite (AcidBir), with a structural formula K$_{0.23}$MnO$_2\cdot$0.43H$_2$O (Zhu *et al.*, 2012), close to that of the crystalline reference KBi8 (K$_{0.24}$MnO$_2\cdot$0.60H$_2$O) (Fig. 3*a* and Table 2). Comparison of their PDFs shows a close resem-

blance of their layer structures, consistent with their nearly identical chemical composition. However, a sharp decrease in the structural coherence is apparent in the PDF of AcidBir at around 7.2 Å, which indicates the presence of stacking disorder (Fig. 10a). To evaluate model fit uncertainty and bias in the PDF analysis of nanomanganates, the original AcidBir PDF was re-analyzed in three ways: (1) with an orthogonal layer cell ($a \neq 3^{1/2}b$) as in the original fit and the initial K and H_2O positions set to the values previously refined (Zhu et al., 2012) (Fig. 10b), (2) a hexagonal layer cell ($a = b$) and the same initial K and H_2O parameter settings (Fig. 10c), and (3) a hexagonal layer cell ($a = b$) and K and H_2O initially positioned as in KBi8 (Fig. 10d and Table S2 in the supplementary materials). The results reported in Table S2 show that the three models give equivalent mathematical solutions. Thus, fitting the whole PDF pattern of c-disordered nanomanganates provides an ambiguous average structure and precludes precise description of local structure. Similarly to disordered

Mn oxides, real-space analysis of HEXS data from disordered Fe oxyhydroxides can be misleading when the model structure is incorrect or the model fit loosely constrained, and is more reliably carried out using Bragg-rod analysis (Drits et al., 1993; Fernandez-Martinez et al., 2010; Manceau, 2011).

In addition to the average structure, Bragg-rod analysis allows size- and strain-broadening effects to be distinguished on the basis of the q dependence of the peak width. The empirical strain function defined in this study, combined with the lognormal modeling of size broadening, can be used to simulate data recorded in the laboratory to q_{max} = 5–6 Å^{-1} because the two effects noticeably and distinctly affect the shape and intensity of the 11 band. Therefore, an important conclusion of this study is that the density of layer vacancies and the positions and numbers of high-Z interlayer cations can be determined without bias simply from the simulation of the 10 and 11 scattering profiles, taking into consideration the microstructure as appropriate, because the structure factor in this q region is a sensitive probe of the average structure. Thus, recording data to higher q is chiefly useful in revealing short-range structure but not so useful for determining the average defective structure of disordered materials. The average nanocrystallite thickness can also be modeled in the most straightforward way using Bragg-rod analysis.

The average structure can be used as a starting model in the DE determination of the shape (morphology) of the real crystallites, suitably with a priori complementary information such as that obtained by transmission electron microscopy. This is performed by the construction of explicit atom-by-atom models that include microstrain effects. The DE intensity curves shown here are averages over many individual variations of the same structure model. One reason why the Bragg-rod method, approximate as it is, is useful for this type of work is that it is fast enough to allow easy interactive adjustment of structures and structural parameters using an ordinary personal computer. With high-performance computing, it will become possible to model structures explicitly using the Debye equation or direct evaluation of the scattering intensity in three-dimensional q space followed by orientational averaging, on an interactive basis. Such modeling will take into account all the factors described herein, such as strain and the need to average over many individual variations of a given structure in order to
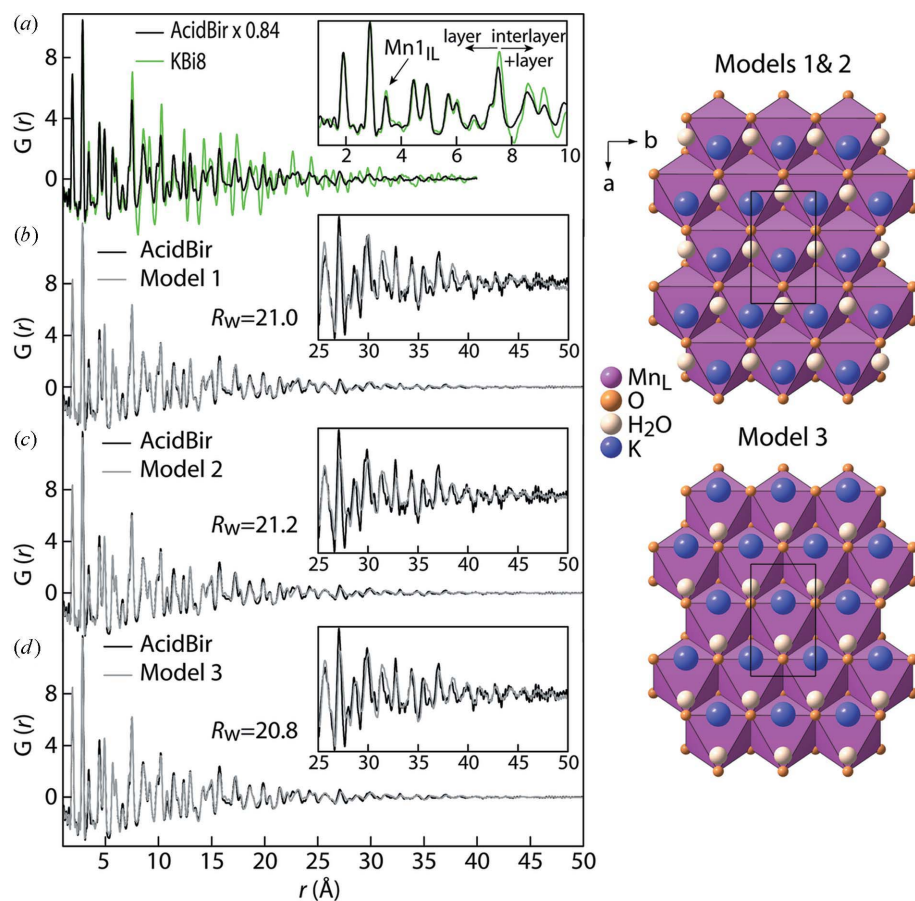
Figure 10
(a) PDFs of AcidBir (data from Zhu et al., 2012) and KBi8. (b)–(d) Three equivalent fits of the AcidBir PDF. Regressed parameter values are given in the supplementary materials, Table S2. (b) Model 1: orthogonal layer cell ($a \neq 3^{1/2}b$) and initial K and H_2O positions set to the values previously refined by Zhu et al. (2012). (c) Model 2: hexagonal layer cell ($a = 3^{1/2}b$) and initial K and H_2O positions set to the values previously refined by Zhu et al. (2012). (d) Model 3: hexagonal layer cell and K and H_2O initially positioned as in KBi8 (Gaillot et al., 2003). The expanded 1.0–10.0 Å region in the top inset shows that AcidBir has a lower Mn···$Mn1_{IL}$ correlation than KBi8, which is consistent with the absence of interlayer Mn in this material (Zhu et al., 2012). It also shows that the two nanomanganates have nearly the same short-range layer structure but a distinctive medium-to-long-range structure above 7.2–7.3 Å because of the turbostratism of AcidBir.

Alain Manceau et al. · Order of phyllomanganate nanoparticles **207**

obtain a representative average. Furthermore, there are systems, such as imogolite tubules, that are not well approximated as flat periodic layers, so the Bragg-rod approach does not apply.

References

Armstrong, A. R. & Bruce, P. G. (1996). *Nature* (*London*), **381**, 499–500.

Bargar, J. R., Fuller, C. C., Marcus, M. A., Brearley, A. J., Perez De la Rosa, M., Webb, S. M. & Caldwell, W. A. (2009). *Geochim. Cosmochim. Acta*, **73**, 889–910.

Beyerlein, K., Cervellino, A., Leoni, M., Snyder, R. L. & Scardi, P. (2009). *Z. Kristallogr. Suppl.* **30**, 85–90.

Billinge, S. J. L. & Kanatzidis, M. G. (2004). *Chem. Commun.* pp. 749–760.

Brock, S. L., Duan, N. G., Tian, Z. R., Giraldo, O., Zhou, H. & Suib, S. L. (1998). *Chem. Mater.* **10**, 2619–2628.

Casas-Cabanas, M., Rodriiguez-Carvajal, J., Canales-Vazquez, J., Laligant, Y., Lacorre, P. & Palacın, M. R. (2007). *J. Power Sources*, **174**, 414–420.

Cernuto, G., Masciocchi, N., Cervellino, A., Colonna, G. M. & Guagliardi, A. (2011). *J. Am. Chem. Soc.* **133**, 3114–3119.

Cervellino, A., Giannini, C. & Guagliardi, A. (2010). *J. Appl. Cryst.* **43**, 1543–1547.

Cheary, R. W. & Coelho, A. (1992). *J. Appl. Cryst.* **25**, 109–121.

Chu, Q., Wang, X., Zhang, X., Li, Q. & Liu, X. (2011). *Inorg. Chem.* **50**, 2049–2051.

Cormie, A., Cross, A., Hollenkamp, A. F. & Donne, S. W. (2010). *Electrochim. Acta*, **55**, 7470–7478.

Debye, P. (1915). *Ann. Phys.* **351**, 809–823.

Drits, V. A., Lanson, B., Bougerol-Chaillout, C., Gorshkov, A. I. & Manceau, A. (2002). *Am. Mineral.* **87**, 1646–1661.

Drits, V. A., Plançon, A., Sakharov, B. A., Besson, G., Tsipursky, S. I. & Tchoubar, C. (1984). *Clay Miner.* **19**, 541–561.

Drits, V. A., Sakharov, B. A., Salyn, A. L. & Manceau, A. (1993). *Clay Miner.* **28**, 185–208.

Drits, V. A., Silvester, E., Gorshkov, A. I. & Manceau, A. (1997). *Am. Mineral.* **82**, 946–961.

Drits, V., Srodon, J. & Eberl, D. D. (1997). *Clays Clay Miner.* **45**, 461–475.

Drits, V. A. & Tchoubar, C. (1990). *X-ray Diffraction by Disordered Lamellar Structures: Theory and Applications to Microdivided Silicates and Carbons.* Berlin: Springer Verlag.

Egami, T. & Billinge, S. J. L. (2003). *Z. Kristallogr. Suppl.* **30**, 85–90.

Farrow, C. L., Juhas, P., Liu, J. W., Bryndin, D., Bozin, E. S., Bloch, J., Proffen, T. & Billinge, S. J. L. (2007). *J. Phys. Condens. Mater.* **19**, 335219.

Feng, Q., Kanoh, H. & Ooi, K. (1999). *J. Mater. Chem.* **9**, 319–333.

Feng, Q., Yanagisawa, K. & Yamasaki, N. (1998). *J. Porous Mater.* **5**, 153–161.

Fernandez-Martinez, A., Timon, V., Roman-Ross, G., Cuello, G. J., Daniels, J. E. & Ayora, C. (2010). *Am. Mineral.* **95**, 1312–1322.

Ferrage, E., Lanson, B., Sakharov, B. A. & Drits, V. A. (2005). *Am. Mineral.* **90**, 1358–1374.

Gaillot, A. C., Drits, V. A., Manceau, A. & Lanson, B. (2007). *Microporous Mesoporous Mater.* **98**, 267–282.

Gaillot, A. C., Drits, V. A., Plançon, A. & Lanson, B. (2004). *Chem. Mater.* **16**, 1890–1905.

Gaillot, A. C., Flot, D., Drits, V. A., Burghammer, M., Manceau, A. & Lanson, B. (2003). *Chem. Mater.* **15**, 4666–4678.

Gateshki, M., Hwang, S. J., Park, D. H., Ren, Y. & Petkov, V. (2004). *J. Phys. Chem. B*, **108**, 14956–14963.

Gelisio, L., Azanza Ricardo, C. L., Leoni, M. & Scardi, P. (2010). *J. Appl. Cryst.* **43**, 647–653.

Gilbert, B. (2008). *J. Appl. Cryst.* **41**, 554–562.

Grangeon, S., Lanson, B., Lanson, M. & Manceau, A. (2008). *Mineral. Mag.* **72**, 1197–1209.

Grangeon, S., Lanson, B., Miyata, N., Tani, Y. & Manceau, A. (2010). *Am. Mineral.* **95**, 1608–1616.

Grangeon, S., Manceau, A., Guilhermet, J., Gaillot, A. C., Lanson, M. & Lanson, L. (2012). *Geochim. Cosmochim. Acta*, **85**, 302–313.

Guinier, A. (1994). *X-ray Diffraction: In Crystals, Imperfect Crystals and Amorphous Bodies.* Mineola: Dover Publications Inc.

Hammersley, A. P., Svensson, S. O., Han, M., Fitch, A. N. & Hausermann, D. (1996). *High Press. Res.* **14**, 235–248.

Hocking, R. K., Brimblecombe, R., Chang, L. Y., Singh, A., Cheah, M. H., Glover, C., Casey, W. H. & Spiccia, L. (2011). *Nat. Chem.* **3**, 461–466.

Jürgensen, A., Widmeyer, J. R., Gordon, R. A., Bendell-Young, L. I., Moore, M. M. & Crozier, E. D. (2004). *Am. Mineral.* **89**, 1110–1118.

Krayzman, V., Levin, I. & Tucker, M. G. (2008). *J. Appl. Cryst.* **41**, 705–714.

Kwon, K. D., Refson, K. & Sposito, G. (2009a). *Geochim. Cosmochim. Acta*, **73**, 4142–4150.

Kwon, K. D., Refson, K. & Sposito, G. (2009b). *Geochim. Cosmochim. Acta*, **73**, 1273–1284.

Kwon, K. D., Refson, K. & Sposito, G. (2010). *Geochim. Cosmochim. Acta*, **74**, 6731–6740.

Laatikainen, K., Pakarinen, J., Laatikainen, M., Koivula, R., Harjula, R. & Paatero, E. (2010). *Sep. Purif. Technol.* **75**, 377–384.

Lafferty, B. J., Ginder-Vogel, M., Zhu, M., Livi, K. J. & Sparks, D. L. (2010). *Environ. Sci. Technol.* **44**, 8467–8472.

Langford, J. I., Louër, D. & Scardi, P. (2000). *J. Appl. Cryst.* **33**, 964–974.

Lanson, B. (2011). *Layered Mineral Structures and their Application in Advanced Technologies*, EMU Notes in Mineralogy No. 11, edited by M. F. Brigatti & A. Mottana, pp. 151–202. London: The Mineralogical Society.

Lanson, B., Drits, V. A., Feng, Q. & Manceau, A. (2002). *Am. Mineral.* **87**, 1662–1671.

Lanson, B., Drits, V. A., Gaillot, A. C., Silvester, E., Plançon, A. & Manceau, A. (2002). *Am. Mineral.* **87**, 1631–1645.

Lanson, B., Drits, V. A., Silvester, E. J. & Manceau, A. (2000). *Am. Mineral.* **85**, 826–835.

Lanson, B., Marcus, M. A., Fakra, S., Panfili, F., Geoffroy, N. & Manceau, A. (2008). *Geochim. Cosmochim. Acta*, **72**, 2478–2490.

Lei, M., de Graff, A. M. R., Thorpe, M. F., Wells, S. A. & Sartbaeva, A. (2009). *Phys. Rev. B*, **80**, 024118.

Leoni, M. (2008). *Z. Kristallogr.* **223**, 561–568.

Li, Y. & Wu, Y. (2009). *Nano Res.* **2**, 54–60.

Li, Z. Q., Lu, C. J., Xia, Z. P., Zhou, Y. & Luo, Z. (2007). *Carbon*, **45**, 1686–1695.

Manceau, A. (2011). *Am. Mineral.* **96**, 521–533.

Manceau, A., Marcus, M. A. & Grangeon, S. (2012) *Am. Mineral.* **97**, 816–827.

Manceau, A., Lanson, B. & Drits, V. A. (2002). *Geochim. Cosmochim. Acta*, **66**, 2639–2663.

Manceau, A., Lanson, M. & Geoffroy, N. (2007). *Geochim. Cosmochim. Acta*, **71**, 95–128.

Masadeh, A. S., Bozin, E. Z., Farrow, C. L., Paglia, G., Juhas, P., Billinge, S. J. L., Karkamkar, A. & Kanatzidis, M. G. (2007). *Phys. Rev. B*, **76**, 115413.

McGreevy, R. L. (2001). *J. Phys. Condens. Matter*, **13**, R877–R913.

Nakayama, M., Shamoto, M. & Kamimura, A. (2010). *Chem. Mater.* **22**, 5887–5894.

Neder, R. B. & Korsunskiy, V. I. (2005). *J. Phys. Condens. Matter*, **17**, S125–S134.

Oddershede, J., Christiansen, T. L. & Ståhl, K. (2008). *J. Appl. Cryst.* **41**, 537–543.

Petkov, V., Cozzoli, P. D., Buonsanti, R., Cingolani, R. & Ren, Y. (2009). *J. Am. Chem. Soc.* **131**, 14264–14266.

Petkov, V., di Francesco, R. G., Billinge, S. J. L., Acharya, M. & Foley, H. C. (1999). *Philos. Mag.* **79**, 1519–1530.

Petkov, V., Ren, Y., Saratovsky, I., Pasten, P., Gurr, S. J., Hayward, M. A., Poeppelmeier, K. R. & Gaillard, J. F. (2009). *ACS Nano*, **3**, 441–445.

Petkov, V., Trikalitis, P. N., Bozin, E. S., Billinge, S. J., Vogt, T. & Kanatzidis, M. G. (2002). *J. Am. Chem. Soc.* **124**, 10157–10162.

Plançon, A. (1981). *J. Appl. Cryst.* **14**, 300–304.

Plançon, A. (2002). *J. Appl. Cryst.* **35**, 377.

Post, J. E. & Appleman, D. E. (1988). *Am. Mineral.* **73**, 1401–1404.

Proffen, T. & Kim, H. (2009). *J. Mater. Chem.* **19**, 5078–5088.

Reynolds, R. C. (1968). *Acta Cryst.* A**24**, 319–320.

Rietveld, H. M. (1969). *J. Appl. Cryst.* **2**, 65–71.

Sakai, N., Ebina, Y., Takada, K. & Sasaki, T. (2005). *J. Electrochem. Soc.* **152**, E384–E389.

Shi, H. S., Reimers, J. N. & Dahn, J. R. (1993). *J. Appl. Cryst.* **26**, 827–836.

Silvester, E., Manceau, A. & Drits, V. A. (1997). *Am. Mineral.* **82**, 962–978.

Simonin, L., Colin, J. F., Ranieri, V., Canevet, E., Martin, J. F., Bourbon, C., Baehtz, C., Strobel, P., Daniel, L. & Patoux, S. (2012). *J. Mater. Chem.* **22**, 11316–11322.

Skanthakumar, S., Antonio, M. R., Wilson, R. E. & Soderholm, L. (2007). *Inorg. Chem.* **46**, 3485–3491.

Skanthakumar, S. & Soderholm, L. (2006). *Mater. Res. Soc. Symp. Proc.* **893**, 411–416.

Soderholm, L., Almond, P. M., Skanthakumar, S., Wilson, R. E. & Burns, P. C. (2008). *Angew. Chem. Int. Ed.* **47**, 493–498.

Soderholm, L., Skanthakumar, S. & Wilson, R. E. (2009). *J. Phys. Chem. A*, **113**, 6391–6397.

Tang, X. H., Li, H. J., Liu, Z. H., Yang, Z. P. & Wang, Z. L. (2010). *J. Power Sources*, **196**, 855–859.

Thackeray, M. M. (1997). *Prog. Solid State Chem.* **25**, 1–71.

Toupin, M., Brousse, T. & Belanger, D. (2004). *Chem. Mater.* **16**, 3184–3190.

Trueblood, K. N., Bürgi, H.-B., Burzlaff, H., Dunitz, J. D., Gramaccioli, C. M., Schulz, H. H., Shmueli, U. & Abrahams, S. C. (1996). *Acta Cryst.* A**52**, 770–781.

Tucker, M. G., Keen, D. A., Dove, M. T., Goodwin, A. L. & Hui, Q. (2007). *J. Phys. Condens. Matter*, **19**, 335218.

Villalobos, M., Lanson, B., Manceau, A., Toner, B. & Sposito, G. (2006). *Am. Mineral.* **91**, 489–502.

Villalobos, M., Toner, B., Bargar, J. & Sposito, G. (2003). *Geochim. Cosmochim. Acta*, **67**, 2649–2662.

Waasmaier, D. & Kirfel, A. (1995). *Acta Cryst.* A**51**, 416–431.

Wagner, C. N. J. (1978). *J. Non-Cryst. Solids*, **31**, 1–40.

Wang, L. Z., Ebina, Y., Takada, K. & Sasaki, T. (2004). *Chem. Commun.* pp. 1074–1075.

Wang, L. Z., Sakai, N., Ebina, Y. & Sasaki, T. (2005). *Chem. Mater.* **17**, 1352–1357.

Weichen, M., Zaharieva, I., Dau, H. & Kurz, P. (2012). *Chem. Sci.* **3**, 2330–2339.

Yan, J., Fan, Z. J., Wei, T., Qian, W. Z., Zhang, M. L. & Wei, F. (2010). *Carbon*, **48**, 3825–3833.

Yang, D. & Frindt, R. F. (1996a). *J. Appl. Phys.* **79**, 2376–2385.

Yang, D. & Frindt, R. F. (1996b). *J. Mater. Res.* **11**, 1733–1738.

Yu, Q., Sasaki, K., Tanaka, K., Ohnuki, T. & Hirajima, T. (2012). *Chem. Geol.* **312**, 106–113.

Zaharieva, I., Chernev, P., Risch, M., Klingan, K., Kohlhoff, M., Fischer, A. & Dau, H. (2012). *Energy Environ. Sci.* **5**, 7081–7089.

Zaleski, J., Wu, G. & Coppens, P. (1998). *J. Appl. Cryst.* **31**, 302–304.

Zhu, M., Farrow, C. L., Post, J. E., Livi, K. J. T., Billinge, S. J. L., Ginder-Vogel, M. & Sparks, D. L. (2012). *Geochim. Cosmochim. Acta*, **81**, 39–55.

Supplementary Materials

Short-range and long-range order of phyllomanganate nanoparticles determined using high energy X-ray scattering

Alain Manceau, Matthew A. Marcus, S. Grangeon, M. Lanson, B. Lanson, A-C. Gaillot, S. Skanthakumar and L. Soderholm

Note S1. Bragg-rod calculation details

In this section, we report selected details of the Bragg-rod calculation that did not appear in the main text, including the consideration of further simulation features not used in the current study but which could be used later to take advantage of the full power of CALCIPOW (Plançon, 2002), if desired. In order to make its use easier, an interactive program ("wrapper") was written in LabVIEW (National Instruments, Austin TX, USA) which generates the input files, calls CALCIPOW, and reads the resulting output. The details to be filled out for each atom in the input file are its occupancy, atomic number, position, and a table of the scattering factor versus $\sin \theta / \lambda$. In addition, there is a section which describes layer stacking because CALCIPOW can handle everything from fully turbostratic layers to fully three-dimensional crystals, with intermediate cases described in terms of random and defined stacking faults (Lanson et al., 2002a). In our case, we only needed the fully-turbostratic description, but the wrapper includes the possibility of the aforementioned types of layer ordering. Similarly, the program can handle the specific case of preferred orientation normal to the scattering vector, so it requires the orientation distribution function as a function of angle from the normal. The program also needs the CSD size and the log-normal distribution parameters for the number of layers per particle, in order to predict the 00l reflections. All of these clerical functions are handled by the wrapper.

In addition, the program requires a table of the T(U) function of Drits and Tchoubar (1990). This function is a scaled Fourier transform of the overlap function of the particle in the transverse dimension. This overlap function represents the fraction of the layer area that is overlapped by a copy of the layer shifted by a given distance. In the case of anisometric particles, T(U) is the orientation average of the Fourier transform of the overlap function with the shift taken in differing directions. To simulate the effect of a distribution of particle size, we considered that the shape of the Bragg rod for a layer of any transverse size is constant, with only the scale factor in q changing. Thus, if the particle is big enough transversely, so that the radius of the Bragg rod is small compared with that of the Ewald sphere, doubling the CSD size in the layer plane will halve the width of the peak in $I(q)$ without changing its shape. This effect may be simulated in CALCIPOW

by replacing T(U) with T(2U), for instance. Thus, if one has a distribution of particle sizes, then T(U) may be replaced by an integral over the distribution $\int d\lambda \, p(\lambda) \mathrm{T}(\mathrm{U}\lambda)$ where $p(\lambda)$ is the probability density function for particles of size λCSD_0, with CSD_0 being the nominal size specified for CALCIPOW. With a log-normal distribution for $p(\lambda)$, we used Gauss-Hermite quadrature to perform the integration and get the effective T(U). If the CSD is circular, that is all we have to do because T(U) for a circle is known analytically. However, for other shapes, one needs to perform other operations to get T(U), which will be summarized only briefly because only circular domains were used in the present investigation. For a general polygonal domain, we can raster the polygon and perform the integral as a sum over line segments, then use Equation 2.20 of Drits and Tchoubar (1990) to calculate the contribution from each line segment. The lengths of these line segments will depend on the direction over which one integrates, hence on the orientation of the scattering vector with respect to the domain. Since we want a powder average, we simply average the T(U) function over a number of angles, typically three.

CALCIPOW allows sites to have fractional occupation, which makes it easy to treat vacancies in an approximate way. However, as mentioned in the main text, if one tries to use the chalcophanite model with ordered vacancies, one winds up with superlattice reflections that are as sharp as the other reflections, whereas the DE model yields only broad bumps due to the short-range nature of the vacancy ordering. Thus, we used the simple unit cell for which parameters are given in Tables 4 and 5.

In order to model strain, we used a *q*-dependent CSD size. The list of reflections is sorted by |*q*|, and a set of CALCIPOW input files is made, one for each value of |*q*|. These files differ only in the list of reflections to be calculated and the CSD. CALCIPOW is then run for each of these files and the resulting intensities added together.

It is probably too complex to implement a stable efficient algorithm for the Bragg-rod fitting that includes all crystallographic, non-uniform, and anisotropic parameters in turbostratic nanocrystals. Therefore, parameter values were optimized by exploring parameter space manually by trial-and-error by varying systematically a set of parameter values. Structural constraints were enforced by varying progressively as a function of pH the amounts of vacancies and interlayer species for the three δ-MnO$_2$ samples, so as to describe these nanomaterials using a unifying framework with only a minimum number of parameters.

Note S2. Debye Equation calculation details

S.2.1. Structural specification

The initial structure is based on a triangular lattice of MnO$_6$ octahedra (the layer), which is truncated to the boundary of the CSD, in our case a circle of a given size. Then, modifications are introduced as follows:

1. Layer vacancies. A given fraction of Mn atoms are left out at random. However, it is assumed for crystal chemical reasons that no two vacancies may be nearest neighbors. Therefore, sets of vacancies are tossed until a structure meeting this condition is found.

2. Vacant sites may be capped with Mn_{IL} atoms. It is forbidden for a vacancy to be capped both above and below, because short-distance Mn_{IL}-Mn_{IL} pairs are excluded from an inspection of the PDF correlations. Each Mn_{IL} atom is provided with three water molecules in the interlayer (represented by oxygens) in addition to the three layer oxygens (O_L) to which it is attached.

3. Interlayer and mid-layer Na and water molecules are added at random sites, making sure that they do not get too close to each other. Minimum distances allowed for atom pairs are Na-(O, water), 2Å, Mn-(O, water), 1.5Å, Na-Mn, 2Å.

4. If it is desired to keep Mn_{IL} from coming too close to each other (see below), then structures are generated according to the above steps until no such unwanted pairs occur.

5. The layer is "bent" to simulate the bending seen in TEM studies. The layer is bent around a spherical or cylindrical mandrel such that the neutral plane is the layer plane $z = 0$. This bending is parameterized by the reciprocal bending radii in x and y directions (supplementary information, note S2).

Because vacancies and all other atoms, except for Mn_L and O_L, occur at random sites, the diffraction from each instance of the structure with given specifications has significant fluctuations. Therefore, we averaged over 100-1000 such structures. This averaging also gives us the opportunity to add polydispersity of layer (CSD) size by generating structures of different sizes for which the intensities are averaged. The positional and "thermal" parameters of the atoms were taken from the Bragg-rod fits.

We did not attempt to model multilayered particles because such modeling would require the explicit generation of atomic positions and interatomic distances for all layers, which would have increased the calculation time and memory requirements by a large factor for a relatively small gain in understanding (the 00l reflections).

S.2.2. Calculation

As Cervellino *et al.* (2010) and others have found, it is impractical to compute the sinc function for each pair of atoms in the double sum over atom pairs and all q-values. Instead, we assembled the distances into a set of histograms, one for each pair of atom types. Here, because atoms of a given element such as Mn, but in different sites (Mn_L, Mn_{IL}), may have different Debye-Waller factors, we counted such atoms as different and assigned them their own histograms. Thus, there is a histogram for Mn_L-O distances, and one for Mn_{IL}-O distances. We took the bin size to be 0.01-0.02 Å. In partial compensation for the discreteness of the histogram bins, we assigned each distance partial membership in the two bins adjacent to it. For example, if there were histogram bins centered at 2.80 Å and 2.81 Å and there was a pair of atoms 2.804 Å apart, we assigned this pair 0.6 membership in the 2.80 Å bin and 0.4 in the 2.81 Å bin. Compared with doing the

exact summation, this procedure is like applying a broadening function with a width that varies depending on how close a distance is to a bin center, but is never more than the bin width. The mean distance in the histogram thus preserves the mean distance in the exact distribution.

We took advantage of the regular tabulation of distances and q-values by using trigonometric recursion relations to compute all values of $\sin(qr)/qr$ once, with minimal evaluation of trig functions. Thus, when computing the diffraction from multiple structures, we only needed calculate these factors once. We then used these factors to compute all values of $f_i f_j \, \text{sinc}(qr)$. The scattering factors f_i for neutral atoms and water molecules (approximated as oxygens) were computed from the Waasmaier and Kirfel (1995) forms as mentioned for the Bragg-rod method. No anomalous dispersion corrections to the coherent atomic scattering factors were introduced.

The description given in the main text is for a model we refer to as "correlated" occupancy, in which each site is either occupied or empty for a given realization of the model, and in which rules about vacancies not neighboring other vacancies and atoms not coming too close to other atoms are obeyed. Another version of the model is what we refer to as "binary" occupancy, in which sites are populated at random, with no regard to crystal-chemical rules. This type of model comes closer to what the Bragg-rod model simulates than does "correlated" occupancy. We also considered "fractional" occupancy, in which we simulate a given probability for each occupied site, with said probability uncorrelated with the occupation of any other site, and perform an analytical average over these occupancies. This can be considered a DE version of the way fractional occupancy is treated in the Bragg-rod case. In this case, we can extend the DE (4) by assuming that each atom i is present with probability p_i, or absent, and that its presence or absence does not affect the position or occupancy of any other site. In that case, we consider the scattering factor f_i to be a random variable which has either its usual value, with probability p_i or vanishes with probability $1 - p_i$, so that the Debye equation is modified to:

$$I = \frac{1}{N_L}\left[\sum_{i=1}^{N_L} p_i \, |f_i|^2 + 2\sum_{i=2}^{N_L}\sum_{j=1}^{i-1} p_{ij} \, \text{Re}(f_i f_j^*)\frac{\sin(q\,|\vec{r}_i - \vec{r}_j|)}{q\,|\vec{r}_i - \vec{r}_j|}\exp\left(-(U_i + U_j)q^2/2\right)\right] \qquad \text{(S1)}$$

where p_{ij} is the probability that both atoms i and j are present. If we assume uncorrelated occupancy, then $p_{ij} = p_i p_j$. Note that $p_{ii} = p_i$, hence the lack of an exponent on p_i in the first term. A comparison of these three modes of modeling for dBi10 and dBi3 is shown in Figure S1. The "binary" and "fractional" models yield near-identical results for the two pH samples, the "correlated " model gives slightly different results at pH 10, and even more so at pH 3 owing to the abundance of Mn_{IL}.
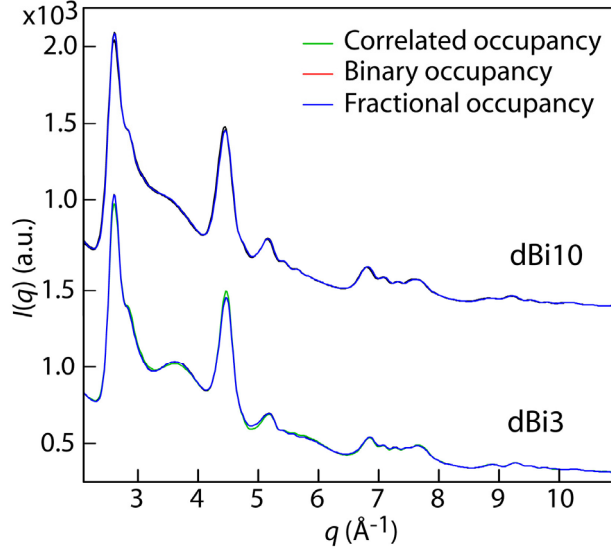
Figure S1. *hk* XRD bands calculated with the strained-layer values given in Table 5 for three possible occupancy models: correlated, binary, and fractional.

S.2.3. Strain

The bending of the layer over a spherical "mandrel" was handled as follows: Let the original Cartesian coordinates of an atom be $x_0 . y_0, z_0$ with the z-axis normal to the layer, and let R_0 be the bend radius. Then, we performed the following set of operations to "wrap" the structure around the sphere of radius R_0:

$$\rho = \sqrt{x_0^2 + y_0^2}$$
$$\theta = \rho / R_0$$
$$R = R_0 + z_0$$
$$x_{bent} = R(x/\rho)\sin\theta \quad y_{bent} = R(y/\rho)\sin\theta$$
$$z_{bent} = z_0 \cos\theta - R_0 \sin^2\theta / (1+\cos\theta) \quad . \tag{S2}$$

The first two lines express the transverse position in polar coordinates. Then, x_{bent}, y_{bent} are computed as the transverse position of the end of an arc that subtends an angle θ as seen from the center of curvature and extending in the azimuthal direction of x_0, y_0. The last line gives the position "above" or "below" the sphere, in a form which does not run into numerical problems at large R_0. Similar formulas can be implemented for cylindrical and ellipsoidal bends.

For a cylindrical bend around the *x*-axis, the corresponding equations are

$$\phi = x_0 / R_0$$
$$R = R_0 + z_0$$
$$x_{bent} = R\sin\phi \tag{S3}$$
$$y_{bent} = y_0$$
$$z_{bent} = z_0 \cos\phi - 2R_0 \sin^2(\phi/2)$$

It should be noted that these forms do not take into account anything about the mechanical properties of the layer. In particular, anticlastic bending is not included in the above cylindrical-bend formulas, and neither bend prescription accounts for Poisson-like coupling of in-plane and out-of-plane strain.

S.2.4. Fitting

In principle, if the experimental measurements were performed on monodisperse single-layer particles, and the background subtracted, then the calculated diffraction intensity should match experiment up to a constant factor. In practice, the contributions from the multi-layered nature of the particles, plus inter-particle interference, means that there will always be a background, assumed to be slowly-varying in q, which the calculation cannot match. Thus, we fit the data using the polynomial form described for the Bragg-rod method (2).

Best fits were found by searching parameter space. We started with the values derived by hand-optimizing the match in the Bragg-rod calculation, after which we did more manual searching, one or two parameters at a time. The obvious thing to try in order to get a better fit than from manual searching is to use a non-derivative minimizer to search parameter space. However, the function being minimized is noisy because of the structure randomness. Thus, we used a brute-force approach in which we defined parameter ranges and simply tossed up to 1000 sets of parameter values within these ranges. This method produced what seems to be a slightly better fit than was obtained in the initial manual searches. By doing such a search over just two parameters at a time (e.g. b and strain), we could fit the normalized sum-squared error (NSS) to a quadratic function of these parameters, thus pinpointing the true minimum and getting an idea of parameter correlations. Because the fractional-occupancy model involves a unique structure for each parameter set, it is faster to compute than either the binary- or correlated-occupancy models and does not introduce statistical noise into the evaluation of the goodness of fit. Therefore, we found it useful to perform the parameter search in the fractional-occupancy model, then redo it in a smaller region of parameter space for the other types of occupancy.

Table S1

Atom parameters from the PDF analysis.

U values for dBi3, dBi6 and dBi10 were averaged, and crystallographic coordinates kept identical at all pHs. O_{IL} are structural water molecules coordinated to Mn_{IL}. Their occupancies are three times the Mn_{IL} occupancy. The Mn_L and Mn_{IL} cation occupancies were linked according to layer-interlayer charge balance, and the Na/K occupancy fixed from chemical analysis (values given in Table 1 for dBi).

	x	y	z	$U_{11,22}$ (Å^2)	U_{33} (Å^2)	Occ.
KBi8 – XRD						
Mn_L	0	0	0			0.88

	x	y	z			
O_L	2/3	1/3	0.070			2.0
Mn_{IL}	0	0	0.150			0.08
O_{IL}	1/3	2/3	1/4			0.24
K	0.24	0.76	1/4			0.23
H_2O	0.225	0.113	1/4			0.36
KBi8 – PDF model 1						
Mn_L	0†	0†	0†	0.003‡[1]	0.012	0.92
O_L	2/3†	1/3†	0.068	0.006	0.029	2.0†
Mn_{IL}	0†	0†	0.150	0.003‡[1]	0.003‡[1]	0.03
O_{IL}	1/3†	2/3†	1/4	0.060‡[2]	0.060‡[2]	0.09
K	0.292§	0.708§	1/4	0.060‡[2]	0.060‡[2]	0.23†
H_2O	0.274§	0.137§	1/4	0.060‡[2]	0.060‡[2]	0.36†
KBi8 – PDF model 2						
Mn_L	0†	0†	0†	0.003‡[1]	0.012	0.92
O_L	2/3†	1/3†	0.068	0.006	0.029	2.0†
Mn_{IL}	0†	0†	0.154	0.003‡[1]	0.003‡[1]	0.03
O_{IL}	1/3†	2/3†	1/4	0.050‡[2]	0.050‡[2]	0.09
K	0.24†	0.76†	1/4	0.050‡[2]	0.050‡[2]	0.23†
H_2O	0.225†	0.113†	1/4	0.050‡[2]	0.050‡[2]	0.36†
NaBi – XRD						
Mn_L	0	0	0			1.0
O_L	0.389	0.627	0.140			2.0
Na_{IL}	0.628	0.476	0.481			0.31
H_2O	0.291	0.180	0.496			0.40
NaBi – Model 1						
Mn_L	0†	0†	0†	0.002	0.016	1.0†
O_L	0.376	0.605	0.134	0.005	0.167	2.0†
Na_{IL}	0.697	0.568	0.510	0.023‡	0.023‡	0.31†
H_2O	0.158	0.199	0.516	0.023‡	0.023‡	0.40†
NaBi – Model 2						
Mn_L	0†	0†	0†	0.002	0.016	1.0†
O_L	0.390	0.626	0.130	0.007	0.104	2.0†
Na_{IL}	0.628†	0.476†	0.481†	0.013‡	0.013‡	0.31†
H_2O	0.291†	0.180†	0.496†	0.013‡	0.013‡	0.40†
dBi						
Mn_L	0.715	0.576	-0.008	0.0012‡[1]	0.0021‡[2]	
O_L	0.525	0.623	0.139	0.0014	0.033	1.0†
O_L	0.250	0.196	0.135	0.0014	0.033	1.0†
O_L	2/3†	1/3†	0.125	0.0014	0.033	1.0†
Mn_{IL}	-0.007	0.017	0.290	0.0012‡[1]	0.0021‡[2]	
O_{IL}	0.179	0.931	0.443	0.0018‡[3]	0.0018‡[3]	
Na	0.950†	0.650†	0.5	0.0018‡[3]	0.0018‡[3]	
Na	0.324	0.963	0.5	0.0018‡[3]	0.0018‡[3]	
H_2O	0.575†	0.260†	0.5	0.0018‡[3]	0.0018‡[3]	1.0†
H_2O	0.425†	0.545†	0.5	0.0018‡[3]	0.0018‡[3]	1.0†

† Fixed. ‡ Kept equal. § Covaried from space group symmetry.

Table S2
Parameters from three equivalent best-fits of the AcidBir PDF in space group $C12/m1$.

c was fixed to 7.32 Å, q_{damp} to 0.045 Å^{-1}, q_{broad} to 0.069 Å^{-1}, Mn_L Occ. to 0.94, K Occ. to 0.26, and H_2O Occ. to 0.77 as in Zhu *et al.* (2012). K and H_2O were allowed to deviate from their mid-layer position to increase the flexibility of the model-fit.

		Parameters from Zhu *et al.* (2012)	Model 1 $(a \neq b\sqrt{3})$ ‡	Model 2 $(a = b\sqrt{3})$ ‡	Model 3 $(a = b\sqrt{3})$ §
a (Å)		4.942	4.919	4.923	4.922
b (Å)		2.829	2.845	-	-
a/b		1.747	1.729	1.732†	1.732†
β (°)		96.02	96.24	96.13	95.75
Scale		1.27	1.36	1.37	1.27
δ_2		3.45	3.28	3.27	3.37
Diameter (Å)		-	78.7	71.8	94.8
Mn_L	U_{11}	0.011	0.002	0.003	0.001
$x=0, y=0, z=0$	U_{22}	0.0029	0.003	0.003	0.005
	U_{33}	0.27	0.163	0.167	0.194
O_L	x	0.349	0.349	0.349	0.347
$y=0$	z	0.131	0.135	0.134	0.134
	U_{11}	0.005	0.005	0.003	0.004
	U_{22}	0.007	0.008	0.009	0.004
	U_{33}	0.11	0.037	0.035	0.033
K	x	0.112	0.141	0.103	0.840
$y=0$	z	0.556	0.506	0.565	0.594
	U_{iso}	0.009	0.079	0.037	0.012
H_2O	x	0.521	0.450	0.497	0.209
$y=0$	z	0.553	0.533	0.547	0.529
	U_{iso}	0.019	0.218	0.010	0.003
R_w (%)		20.8	21.0	21.2	20.8

‡ K, H_2O positions close to Zhu *et al.* (2012). § K, H_2O positions close to KBi8. † Fixed.